Thomas Kämpfe

Electron Devices Based On Ferroelectric Hafnium Oxide Thin Films

TUDpress

DRESDNER BEITRÄGE ZUR SENSORIK

Herausgegeben von
Gerald Gerlach

Band 85

Thomas Kämpfe

ELECTRON DEVICES BASED ON FERROELECTRIC HAFNIUM OXIDE THIN FILMS

TUDpress
2022

This thesis was published under the title „ Electron Devices based on Ferroelectric Hafnium Oxide Thin Films" on December 16, 2021 as an habilitation thesis at the Faculty of Electrical Engineering and Information Technology of the Dresden University of Technology and defended on 28.07.2022.

Chairman: Prof. Dr.-Ing. Thomas Mikolajick
Reviewer: Prof. Dr.-Ing. habil. Gerald Gerlach
Prof. Dr. Kai Ni
Prof. Dr. Xueqing Li
Prof. Dr. rer. nat. habil. Elizabeth von Hauff
Prof. Dr.-Ing. habil. Christian Georg Mayr
Prof. Dr. rer. nat. Stefan Mannsfeld
Prof. Dr. rer. nat. Johann W. Bartha

Bibliografische Information der Deutschen Nationalbibliothek
Die Deutsche Nationalbibliothek verzeichnet diese Publikation in der Deutschen Nationalbibliografie; detaillierte bibliografische Daten sind im Internet über http://dnb.d-nb.de abrufbar.

Bibliographic information published by the Deutsche Nationalbibliothek
The Deutsche Nationalbibliothek lists this publication in the Deutsche Nationalbibliografie; detailed bibliographic data are available in the Internet at http://dnb.d-nb.de.

ISBN 978-3-95908-552-6

Thomas Kämpfe: *Electron Devices Based on Ferroelectric Hafnium Oxide Thin Films*, © October 2022

© TUDPress
Thelem Universitätsverlag und
Buchhandlung GmbH & Co. KG
Dresden
Tel.: 0351/472 14 63 | Fax: 0351/479 69 721
http://www.tudpress.de

TUDpress ist ein Imprint von Thelem.
Alle Rechte vorbehalten. All rights reserved.
Gesetzt vom Autor.
Printed in Germany.

CONTENTS

I INTRODUCTION 1

II STRUCTURAL & FERROELECTRIC PROPERTIES 5

1 FERROELECTRIC THIN FILMS 7
1.1 History of ferroelectric materials 7
1.2 Deposition of ultra-thin ferroelectric films 9
Publication: Doping ferroelectric hafnium oxide by in-situ precursor mixing 11

2 STRUCTURAL PROPERTIES 19
2.1 Ferroelectricity as a structural property 19
2.2 Texture analysis on titanium nitride substrate 25
Publication: Local crystallographic phase detection and texture mapping in ferroelectric Zr doped HfO_2 films by transmission-EBSD 29
2.3 Texture analysis on silicon interface layers 34
Publication: Impact of the SiO_2 interface layer on the crystallographic texture of ferroelectric hafnium oxide 35
2.4 Texture analysis within integrated devices 41
Publication: Structural and electrical comparison of Si and Zr doped hafnium oxide thin films and integrated FeFETs utilizing transmission Kikuchi diffraction 41
2.5 Wake-up effect and electric field-induced crystallization 54
Publication: On the origin of wake-up in ferroelectric hafnium oxide 56
Publication: Electric field-induced crystallization of ferroelectric hafnium zirconium oxide 64

III MEMORY DEVICES & APPLICATIONS 71

3 CAPACITIVE & RESISTIVE MEMORIES 73
3.1 Back-end of line (BEOL) integration 74
Publication: Back-end-of-line compatible low temperature furnace anneal for ferroelectric hafnium zirconium oxide formation . 77
3.2 Radiation aspects 83
Publication: Heavy ion irradiation effects on structural and ferroelectric properties of HfO_2 films 86
3.3 Ferroelectric tunnel junctions (FTJ) 89

Publication: Impact of the ferroelectric and interface layer optimization in an MFIS HZO based ferroelectric tunnel junction for neuromorphic based synaptic storage 91
4 TRANSISTOR MEMORIES 93
4.1 Ferroelectric field-effect transistors 93
4.2 Interface layer optimization 97
Publication: High endurance ferroelectric hafnium oxide-based FeFET memory without retention penalty 100
4.3 Non-volatile CMOS 106
Publication: Integration of hafnium oxide on epitaxial SiGe for p-type ferroelectric FET application 108
4.4 Temperature influences 112
Publication: A study on the temperature-dependent operation of fluorite-structure-based ferroelectric HfO_2 memory FeFET: a temperature-modulated operation 114
Publication: A study on the temperature-dependent operation of fluorite-structure-based ferroelectric HfO_2 memory FeFET: pyroelectricity and reliability 121
4.5 Multi-level cells (MLC) 128
Publication: Ferroelectric field effect transistors as a synapse for neuromorphic application 130
Publication: Influence of microstructure on the variability and current percolation paths in ferroelectric hafnium oxide based neuromorphic FeFET synapses 136
5 EDGE AND ARTIFICIAL INTELLIGENCE 139
5.1 In-Memory Computing 142
Publication: A ferroelectric FET based in-memory architecture for multi-precision neural networks 148
Publication: Ultra-low power flexible precision FeFET based analog in-memory computing 154
5.2 Computing with associative memories 158
Publication: A scalable design of multi-bit ferroelectric content addressable memory for data-centric computing 162
Publication: In-memory nearest neighbor search with FeFET multi-bit content-addressable memories 166

IV BEYOND-MEMORY DEVICES & APPLICATIONS 173
6 PYROELECTRIC AND ELECTROCALORIC PROPERTIES & DEVICES 175
6.1 Pyroelectric properties 175

Publication: Layer thickness scaling and wake-up effect of pyroelectric response in Si-doped HfO_2 . . . 180
Publication: Frequency domain analysis of pyroelectric response in silicon doped hafnium oxide . . . 185
Publication: Enhanced pyroelectric response at morphotropic and field-induced phase transitions in ferroelectric hafnium oxide thin films . . . 190
6.2 Pyroelectric energy harvesting . . . 197
Publication: Energy harvesting in the back-end of line with CMOS compatible ferroelectric hafnium oxide . . . 199
Publication: Pyroelectric energy conversion in doped hafnium oxide (HfO_2) thin films on area-enhanced substrates . . . 203
6.3 Electrocaloric properties and cooling applications . . . 210
Publication: The electrocaloric effect in doped hafnium oxide: Comparison of direct and indirect measurements . . . 212
7 PIEZOELECTRIC PROPERTIES & DEVICES 217
7.1 Piezoelectric properties & applications . . . 217
Publication: Piezoelectric response of polycrystalline silicon-doped hafnium oxide thin films determined by rapid temperature cycles . . . 219
8 DIELECTRIC PROPERTIES & APPLICATIONS 225
8.1 Thin-film varactors . . . 225
Publication: Tunability of ferroelectric hafnium zirconium oxide for varactor a pplications . . . 229
Publication: RF-characterization of ferroelectric hafnium zirconium oxide varactors . . . 237
8.2 Applications of thin-film varactors . . . 246
Publication: A tunable mmWave band-pass filter based on ferroelectric hafnium zirconium oxide varactors . . . 248
Publication: Investigation of BEoL integrated ferroelectric thin-film HfO2 for mmWave varactor applications . . . 251

V CONCLUSION & OUTLOOK 255

Appendix 259

BIBLIOGRAPHY 261
PUBLICATION LIST 281
ACKNOWLEDGMENTS 303

ABSTRACT

The discovery of ferroelectric hafnium oxide revived the research on ferroelectric integrated devices in microelectronics for memory, radio frequency as well as piezoelectric or pyroelectric applications.

In this habilitation thesis we want to cover a broad scope on the research which was undertaken towards application of integrated ferroelectric hafnium oxide electron devices for microelectronics at the Fraunhofer IPMS, Center Nanoelectronic Technologies (CNT) within various projects, mostly managed by the author.

We start from the theoretical aspects of ferroelectric thin films, which covers the discussion of basic physical laws governing ferroelectrics as well as domains. Furthermore, we present the structural aspects relevant for hafnium oxide thin films particularly investigated under device aspects as well as novel measurement techniques which can be applied to study such films and integrated devices. We will also discuss an effect often observed in hafnium oxide based ferroelectrics, the wake-up effect.

We present the relevant ferroelectric memory device concepts, which have been revived by the discovery of ferroelectric hafnium oxide, their integration as well as the suitable figures of merits for these various ferroelectric memory concepts, with an emphasis on ferroelectric field effect transistors, random access memories and tunnel junctions.

The application of novel memory concepts for edge computing via analog in-memory computing will be discussed. We will introduce an architecture, which can calculate convolutional neural networks with very high energy efficiency and makes use of bit decomposition to improve the reliability of the multiply-and-accumulate computations executed by the AND gate memory array. We will also introduce an associative memory array, which is capable to yield comparison of an input query vector with stored vectors in the array and is composed of ternary content-addressable memory bitcells.

Further properties of ferroelectric materials such as its pyroelectric and piezoelectric properties are investigated. We will discuss the pyroelectric properties in hafnium oxide for infrared sensors and how it can be utilized for energy harvesting. The closely associated electrocaloric properties are discussed, which can be applied in miniaturized cooling systems.

In the last chapter we will discuss the tunable dielectric properties, which we will discuss in the context of tunable microwave passives. We will present simulation and experimental implementations of phase shifters and bandpass filters.

ZUSAMMENFASSUNG

Die Entdeckung des ferroelektrischen Hafniumoxids hat die Forschung zu integrierten ferroelektrischen Bauelementen in der Mikroelektronik für Speicher-, Hochfrequenz- sowie piezoelektrische und pyroelektrische Anwendungen neu belebt.

In dieser Habilitationsschrift soll ein breiter Überblick über die Forschungsarbeiten gegeben werden, die am Fraunhofer IPMS, Center Nanoelectronic Technologies (CNT) im Rahmen verschiedener, meist vom Autor geleiteter Projekte zur Anwendung integrierter ferroelektrischer Hafniumoxid-Elektronenbauelemente für die Mikroelektronik durchgeführt wurden.

Wir beginnen mit den theoretischen Aspekten ferroelektrischer Dünnschichten, der Diskussion grundlegender physikalischer Gesetze für Ferroelektrika sowie Domänen. Darüber hinaus werden die strukturellen Aspekte vorgestellt, die für Hafniumoxid-Dünnschichten relevant sind insbesondere unter Bauelementaspekten als auch neuartige Messverfahren, die zur Untersuchung solcher Schichten und integrierter Bauelemente eingesetzt werden können. Wir werden auch einen Effekt erörtern, der häufig in Ferroelektrika auf Hafniumoxidbasis beobachtet wird, den Wake-up-Effekt.

Die relevanten ferroelektrischen Speicherkonzepte werden eingeführt, die durch die Entdeckung von ferroelektrischem Hafniumoxid wiederbelebt wurden, ihre Integration sowie die geeigneten Kennzahlen für diese verschiedenen ferroelektrischen Speicherkonzepte, wobei der Schwerpunkt auf ferroelektrischen Feldeffekttransistoren, Direktzugriffsspeichern und Tunnelübergängsspeichern liegt.

Die Anwendung neuartiger Speicherkonzepte für Edge Computing durch analoges In-Memory-Computing wird diskutiert. Wir stellen eine Architektur vor, die faltbare neuronale Netze mit sehr hoher Energieeffizienz berechnen kann sowie Bit-Zerlegung nutzt, um die Zuverlässigkeit der Multiplikations- und Akkumulationsberechnungen zu verbessern, die von der AND-Gatter-Speicheranordnung ausgeführt werden. Wir werden auch ein assoziatives Speicherarray vorstellen, das in der Lage ist, einen Vergleich eines Eingabeabfragevektors mit gespeicherten Vektoren im Array durchzuführen, und das aus ternären inhaltsadressierbaren Speicher-Bitzellen besteht.

Weitere Eigenschaften ferroelektrischer Materialien wie ihre pyroelektrischen und piezoelektrischen Eigenschaften werden untersucht. Wir werden die pyro-

elektrischen Eigenschaften von Hafniumoxid für Infrarotsensoren erörtern und wie sie für das Energy Harvesting genutzt werden können. Die eng damit verbundenen elektrokalorischen Eigenschaften werden erörtert, die in miniaturisierten Kühlsystemen angewendet werden können.

Im letzten Kapitel werden wir die abstimmbaren dielektrischen Eigenschaften erörtern, die wir im Zusammenhang mit abstimmbaren Mikrowellen-Passiven diskutieren werden. Wir werden Simulationen und experimentelle Implementierungen von Phasenschiebern und Bandpassfiltern vorstellen.

Part I

INTRODUCTION

INTRODUCTION

In this chapter, we want to motivate the work from different perspectives. We want to introduce the novel ferroelectric material hafnium oxide and the scope of applications for electron devices it can offer and particularly how this can support or enrich the advancement of Moore's law.

100 YEARS OF FERROELECTRICITY - 10 YEARS OF FERROELECTRIC HAFNIUM OXIDE This thesis was planned, when we celebrated the 100 years anniversary of the discovery of ferroelectricity by Joseph Valasek in 1921 [1]. Various materials have been found since the first - Rochelle salt - featured the ferroelectric phenomena. These materials have been shown to be applied in a broad range of applications from actuators via capacitors to non-volatile memories (NVM) such as ferroelectric random-access memories (FRAM) and ferroelectric field effect transistors. Despite the very interesting behavior, the difficult implementation into high-volume complementary metal oxide semiconductor (CMOS) fabrication processes, which are connected with high anneal temperatures, necessary film thickness, etch characteristics and/or elementary contamination control, impedimented the large-scale application in microelectronics despite niche implementations. However, 10 years ago ferroelectric hafnium oxide has been reported for ultra-thin films, which has the prospect to change this status quo. Particularly, HfO_2 thin films exhibit some unique properties such as scale-free nano-ferroelectricity without a super-paraelectric limit and a high coercive field in the order of 1 $MVcm^{-1}$ [2, 3].

CMOS-COMPATIBLE FERROELECTRICS Upon scaling of metal-oxide-semiconductor field effect transistors (MOSFETs) a strong demand to increase the permittivity of the gate oxide was observed to still preserve channel control for short-channel devices. Various (oxide) materials with a permittivity higher than silicon oxide have been investigated, among these also HfO_2. Various crystallographic phases for bulk HfO_2 dielectrics were known such as monoclinic, tetragonal and cubic [4] with the monoclinic phase known to be the stable ground state. However, for thin films further influences such as film stress, thermal quenching, interface formation, polycrystallinity etc. were expected to have an influence on the scaling of nanoelectronic devices. Hence, an amorphous film was targeted, e.g. by additional doping with silicon, to obtain better film homogeneity. However, for larger film thicknesses such as 10 nm, which still resembles an ultra-thin film, a hysteresis loop of the capacitance-voltage curve was observed indicating the appearance

of ferroelectricity in these crystallized films [5]. Further studies confirmed the existence of the ferroelectricity in HfO_2 thin films, creating the first truly CMOS compatible ferroelectric materials after the large-scale implementation of high-k materials into metal-oxide-semiconductor field effect transistors (MOSFETs) at about 2010, starting from the 28 nm technology node.

EDGE INTELLIGENCE The future data-centered world requires a kind of intelligence of edge devices or edge intelligence (EI), the ability to analyze data locally and to decide on a course of action autonomously. The obvious present challenges with Moore's law scaling and limitations of the conventional von Neumann computing architectures are limiting the performance and energy efficiency of such an implementation. The discovery of the advanced CMOS-compatible HfO_2-based ferroelectric devices promises to open the door for a new type of electronics: ferroelectronics; electronics based on ferroelectric building blocks integrated on advanced CMOS technology nodes. It promises to enable much-needed improvement in computing capabilities making EI a reality. In-memory computing in data-flow architectures is at the core of ferroelectronics. It could enable building 1000× more compute energy-efficient small-system artificial intelligence (AI) engines needed for EI. Smart IoT devices enable new applications, for example, micro drones, that demand higher performance to support locally embedded intelligence, real-time learning, and autonomy. They could drive the next phase of growth in the semiconductor industry.

MORE THAN MOORE Further interesting properties of ferroelectric materials such as large pyroelectric and piezoelectric properties are attractive, particularly in conjunction with CMOS-compatibility, which offers further possibilities for low-cost, microscopic integration. That includes pyroelectric infrared sensors, piezoelectric micro-electromachined ultrasound transducers (PMUT) or high-frequency filters, pyroelectric and piezoelectric energy harvesters as well as electrocaloric cooling systems. Furthermore, the tunable dielectric properties can be used for tunable microwave passives such as delay-lines, phase shifters, bandpass filters or voltage-controlled oscillators.

Part II

STRUCTURAL & FERROELECTRIC PROPERTIES

1 FERROELECTRIC THIN FILMS

In this chapter, the material properties of ferroelectricity will be discussed. The theoretical framework will be briefly introduced, which includes typical characteristics of ferroelectric materials.

1.1 HISTORY OF FERROELECTRIC MATERIALS

Ferroelectric materials show a reversible spontaneous polarization when subject to external electric fields. This phenomenon was first observed by the PhD student Joseph Valasek in 1921, who noticed hysteretic loops of the induced dielectric polarization upon applied electric fields in Rochelle salt/$C_4H_4KNaO_6$ [1] [6, 7], investigating them as a piezoelectric to detect earthquakes[2]. However, this discovery went largely unrecognized at the time.

For almost 15 years, ferroelectricity was considered as a very specific property in Rochelle salt[3], until Busch and Scherrer discovered ferroelectricity in potassium dihydrogen phosphate/KH_2PO_4 (KDP) in 1935. During World War II, the anomalous dielectric properties of barium titanate/$BaTiO_3$ (BTO) were discovered in ceramic specimens independently by Wainer and Solomon in the USA, by Ogawa in Japan, and by Wul and Goldman in the Soviet Union [8–11]. Unlike Rochelle salt, BTO and KDP are insoluble in water, chemically stable at room temperature, and have much better electrical and mechanical properties.

Since then, many ferroelectric materials have been discovered and the research activity has rapidly increased. The most common ferroelectric single crystals nowadays are lithium niobate/$LiNbO_3$ (LNO) [12], barium titanate/$BaTiO_3$ (BTO) [12, 13], strontium barium niobate/$Sr_xBa_{1-x}Nb_2O_6$ (SBN) [14–16], and lithium tantalate/ $LiTaO_3$ (LTO). With modern evaporation techniques, typically pulsed laser deposition (PLD) [17], atomic layer deposition (ALD) [18], or RF magnetron sputtering [19], ferroelectric thin films have been fabricated. The most studied ferroelectric thin films are BFO [20, 21] and lead zirconate titanate/$Pb(Zr_xTi_{1-x})O_3$ (PZT)

1 Also referred as Seignette salt as being first synthesized in the 17th century by Pierre Seignette in La Rochelle, France from wine.

2 Piezoelectric materials were already known by the time. This phenomenon will be discussed in detail in Sec. 7

3 As Vitaly Ginzburg looked into this effect more detailed from a theoretical solid-state physics point of view, he still coined it Seignetteoelectric

[22–25]. Apart from these oxide materials antimony sulphoiodide/SbSI [26, 27], triglycine sulfate/$(NH_2CH_2COOH)_3 \cdot H_2SO_4$ (TGS) [28, 29], as well as the polymer polyvinylidene fluoride (PVDF) [30–38] are of importance and investigated already for several decades.

Despite the very interesting behavior of the aforementioned ferroelectric materials and the large scale implementation in various applications such as storage capacitors or actuators, only a few examples are known for an implementation into nanoelectronic systems, which is mainly a result of the CMOS[4] non-compatibility of these materials. Reasons for this can be the high anneal temperature or the specifically required electrode materials. Electrode materials can be detrimental due to diffusion, support of the creation of deep traps or electromigration, which have a strong influence in the reliability of VLSI systems.

Nevertheless, examples of such microelectronic implementations are SBN or PZT for ferroelectric random access memory (FRAM), PZT for piezoelectric microelectromechanical systems (MEMS) or BST for thin-film varactors. The latter two are merely not co-integrated with MOSFETs and are hence not genuinely disturbed by non-CMOS compatibility. Despite the integration of strontium barium niobate/$Sr_xBa_{1-x}Nb_2O_6$ (SBN) or PZT for the non-volatile memory FRAM, in the 2000's it showed to be difficult to further scale the memory cell form factor. One major disadvantage was the difficulty to further scale the film thickness below 100nm, which made a very small capacitor integration challenging, e.g. with regard to film etching due to the high aspect ratios. Yet, FRAM is still a commercially available memory cell despite its meanwhile comparably high cost, due to its remarkable endurance and low-power properties.

In recent years, several ultra-thin film or two-dimensional (2D) ferroelectric materials have been reported, such as $In2Se_3$ monolayers [39], topological ferroelectrics at the surface of $SrTiO_3$ [40], wurtzite-type AlScN [41] and ultra-thin HfO_2 films [42], among which the latter is currently expected to be the most promising for various applications and which is also the major topic of this book.

The ferroelectricity in hafnium oxide/HfO_2 (HFO) was discovered in 2007 within the research & development team of the memory company Qimonda, studying high-k materials. Hereby, high-k materials are materials with an increased k-value as compared to the standard oxides used in nanoelectronic systems, such as silicon oxide or silicon oxynitride. HFO by then was considered a very promising candidate to replace the silicon oxynitride within metal-oxide-semiconductor field effect transistors (MOSFETs), with a permittivity of about ten times larger than sil-

4 CMOS stands for complementary MOSFET and describes the current state-of-the-art implementation in very large scale integration (VLSI) of transistors in microchips.

icon oxide. Finally, it was actually also used and is currently implemented in all newer technology nodes from 28 nm onwards.

Recently, also bulk ferroelectric crystals of HfO_2 [43] were grown by floating-zone technique, which support the idea of ferroelectricity in HfO_2 being a structural property rather than an interfacial effect.

1.2 DEPOSITION OF ULTRA-THIN FERROELECTRIC FILMS

Since the discovery, the majority of studies on ferroelectric HfO_2 ultra-thin films have been carried out on films fabricated by atomic layer deposition (ALD).

ALD of HfO_2 thin films is already investigated for about 2-3 decades for the implementation as high-k oxide for MOSFET devices as for thicknesses of the gate oxide SiO_2 below 20 Å, when tunneling currents through the gate dielectric became substantial. HfO_2 was found to be an excellent candidate due to its high dielectric constant and nominal stability on Si/SiON interfaces. To fulfill the large requirements with respect to thickness precision and uniformity in front-end-of-line (FEOL) CMOS implementation, ALD techniques were developed.

ALD is a special thin-film deposition technique, which is based on the sequential use of a gas-phase chemical process and more precisely a subset of chemical vapour deposition (CVD), employing precursors. These precursors react with the surface of a material once at a time in a sequential, self-limiting manner. Between the deposition steps, one typically applies a purge step with an inert gas such as Ar. A thin film is slowly deposited through repeated exposure to separate precursors. In the case of HfO_2 several precursors have been used, e.g. tetrakis (ethylmethylamido) hafnium(IV)/TEMAHf or $HfCl_4$ and ozone as the oxidizing agent. The deposition temperature is typically slightly below 200°C.

Recently, further deposition techniques have been studied such as pulsed-laser deposition (PLD) and physical vapor deposition (PVD) for ferroelectric HfO_2 and ZrO_2 films [45, 46]. PLD of $HfZrO_2$ has been shown on various templates such as $LaSrMnO_2$ and $YSrZrO_2$, creating epitaxial films [47, 48]. However, these templates are not compatible with standard CMOS microelectronic integration. Hence, PLD was also investigated on more conventional substrates and showed epitaxial growth to some extent on such Si/SiO_2 interfaces [49]. Despite these findings to be interesting as an outlook in terms of yield progression with quasi-epitaxial films, still, PLD techniques often result in large-particle generation impedimenting microelectronic application. PVD methods have the advantage to reduce the necessary deposition temperature down to room temperature, which can impediment nanogranular crystallization inside the film. Hence, particularly, PVD techniques

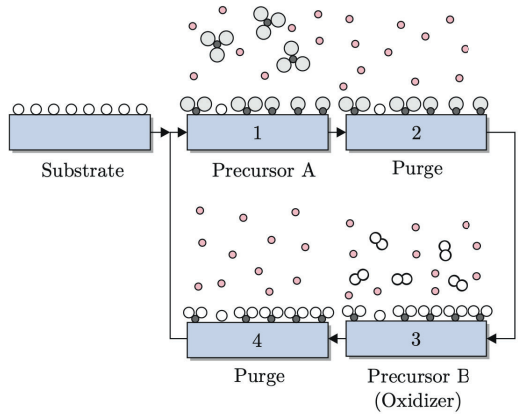

Figure 1: Schematic view of an ALD process. Steps 1 to 4 are repeated to achieve the desired film thickness. Reprinted with permission from [44].

could be further interesting for implementation into microelectronic processes due to their inherent fast film growth and ability to obtain suitable film homogeneity as well as the possibility to create thicker ferroelectric films. However, particularly for ultra-thin films, PVD is expected to be limited with respect to film uniformity.

PUBLICATION: DOPING FERROELECTRIC HAFNIUM OXIDE BY IN-SITU PRECURSOR MIXING

Despite the demonstration of further film deposition techniques, ALD is still the dominant film deposition technique applied to realize ferroelectric HfO_2 ultra-thin films due to the precise deposition mechanism. Necessary doping of the HfO_2 layers in ALD processes is hereby typically achieved by a sequential deposition of SiO_2, Al_2O_3 and La_2O_3 layers. In our case, the precursors tris (dimethylamino) silane(3DMAS), trimethyl aluminum (TMA) and tris (isopropyl cyclopentadienyl) lanthanum (La-(iPrCp)$_3$) were used. The cycle ratio finally defines the achievable doping concentration.

However, as various dopants such as Si and Al actually require quite low concentrations of just some cat% to achieve a suitable spontaneous polarization, often only a few dopant ALD cycles are sufficient. This is contradictory to a good intermixing between the HfO_2 matrix and the dopant species. So far, little is known

about the impact of dopant distribution throughout the depth of HfO_2 thin films. Techniques such as time-of-flight secondary ion mass spectroscopy (ToF SIMS) do not provide sufficient depth resolution. However, it was found that an inhomogeneous dopant concentration can significantly reduce the remanent polarization. Further, doping has an influence on the defect chemistry, thus creating internal bias fields in the ferroelectric thin films, which directly influence switchable polarization, fatigue, and wake-up effects in the material. Charged defect sites can lead to pinned domains, which require extensive electric field cycling to switch. Therefore, in this work, some films are manufactured by intermixing various precursors in the process chamber. The process has been suggested for lithium-based films first, and a more detailed description for HfO_2-based films has been published in Reference.

Due to this cycled deposition, only very few dopant concentration values can be realized due to minimum film thickness of the dopant interlayer. Hence, a tailored fabrication process with *in-situ* intermixing various precursors during ALD to study the effect of dopant distribution on the physical and electrical film properties has been employed [50]. Three common dopants have been analyzed: trivalent Al and La as well as tetravalent Si. In this modified ALD process, the metal-organic precursor species are mixed on the substrate surface to achieve homogeneous films with low defect density and significantly reduced internal bias fields have been analyzed.

Furthermore, plasma enhanced ALD deposition can increase cross-wafer uniformity [51].

PUBLICATION: Doping ferroelectric hafnium oxide by in-situ precursor mixing

PUBLICATION DETAILS The following publication is reproduced with permission from: C. Mart, K. Kühnel, T. Kämpfe, M. Czernohorsky, M. Wiatr, S. Kolodinski, and W. Weinreich, "Doping ferroelectric hafnium oxide by in-situ precursor mixing", ACS Applied Electronic Materials 1, 2612-2618 (2019). Copyright 2019 American Chemical Society.

ACS APPLIED ELECTRONIC MATERIALS

Article

Cite This: ACS Appl. Electron. Mater. 2019, 1, 2612−2618

pubs.acs.org/acsaelm

Doping Ferroelectric Hafnium Oxide by in-Situ Precursor Mixing

Clemens Mart,*[,†,‡] Kati Kühnel,[†] Thomas Kämpfe,[†] Malte Czernohorsky,[†] Maciej Wiatr,[§] Sabine Kolodinski,[§] and Wenke Weinreich[†]

[†]Fraunhofer Institute for Photonic Microsystems IPMS, Königsbrücker Str. 178, 01099 Dresden, Germany

[‡]Institute of Applied Physics, Technische Universität Dresden, 01062 Dresden, Germany

[§]GLOBALFOUNDRIES Management Services LLC & Co. KG, Wilschdorfer Landstraße 101, 01109 Dresden, Germany

Supporting Information

ABSTRACT: We employ a modified atomic layer deposition process utilizing in-situ mixing of precursors to obtain doped hafnium oxide thin films with improved ferroelectric properties. The method is demonstrated with aluminum, silicon, and lanthanum doping, where film composition and crystal structure are analyzed. With the modified process, low dopant concentrations are shown to be accessible, and improved wafer-level uniformity of dopant concentration is demonstrated for Si and La doping. Characterization of the ferroelectric hysteresis confirms increased remanent polarization values with the modified process variant for all examined dopants. The switching density of the 10 nm thick films is analyzed by using first-order reversal curve measurements, where confined peaks are observed, which are an indication of low defect density and reduced internal bias fields. Emerging applications of doped hafnium oxide thin films such as nonvolatile memory, infrared sensors, or neuromorphic devices may benefit from the enhanced stoichiometry control and film properties by using the proposed deposition method.

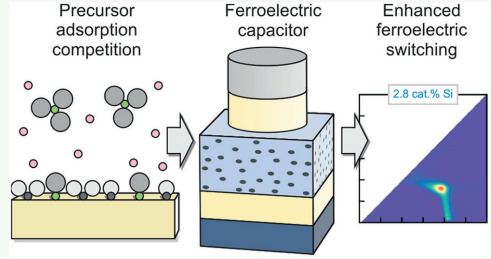

KEYWORDS: *atomic layer deposition, ferroelectrics, thin films, precursor, hafnium oxide, doping*

INTRODUCTION

Since the discovery of ferroelectricity in doped hafnium oxide thin films in 2011,[1] an increasing number of publications have assessed the formation of the polar orthorhombic phase as the premise for spontaneous polarization. Many factors impact the electrical performance of these films, such as thickness,[2] mechanical stress,[3] and defect chemistry.[4,5] However, adding dopants such as Si, Y, La, Al, or Gd remains the most direct and robust way to achieve ferroelectricity in hafnium oxide.[6]

Doped hafnium oxide thin films are commonly manufactured by using atomic layer deposition, where precursors are injected into the process chamber sequentially, each followed by purging with an inert gas. HfO_2 and dopant deposition pulses are alternated in a nanolamination technique to achieve the desired stoichiometry.[7] Many dopants such as Si and Al require low concentrations of <4 cat. % to achieve a large spontaneous polarization,[8,9] and often only few dopant ALD cycles are sufficient. This is contradictory to a good intermixing between the HfO_2 matrix and the dopant species. Researchers may resort to artificially reducing the growth per dopant ALD cycle to enhance the distribution, e.g., by using short precursor pulse times or operating outside of the ideal ALD process window. However, this implicates reduced wafer-level uniformity of stoichiometry and electrical parameters, which is a challenge especially when researching materials for state-of-the-art 300 mm substrates in emerging applications such as nonvolatile memory,[10] energy storage,[11] infrared sensors,[12] or neuromorphic devices.[13]

Little is known about the impact of dopant distribution throughout the depth of HfO_2 thin films. Lomenzo et al. found that an inhomogeneous dopant concentration effectively lowers the remanent polarization.[14] Earlier works have also shown that doping impacts the defect chemistry,[15] thus creating internal bias fields in the ferroelectric thin films, which directly influence switchable polarization, fatigue, and wake-up effects in the material.[16,17] Charged defect sites can lead to pinned domains, which require extensive electric field cycling to switch.[18]

In this work, we employ a tailored fabrication process with in-situ intermixing of precursors during ALD to study the effect of dopant distribution on the physical and electrical film properties. We analyze three common dopants: trivalent Al and La as well as tetravalent Si. In this modified ALD process, the metal−organic precursor species are mixed on the substrate surface to achieve homogeneous films with low defect density and significantly reduced internal bias fields. One work employing a similar technique showed promising results for the deposition of ternary lithium titanate films,[19]

Received: September 12, 2019
Accepted: November 12, 2019
Published: November 12, 2019

Downloaded via SLUB DRESDEN on January 15, 2020 at 13:30:53 (UTC).
See https://pubs.acs.org/sharingguidelines for options on how to legitimately share published articles.

 © 2019 American Chemical Society

DOI: 10.1021/acsaelm.9b00591
ACS Appl. Electron. Mater. 2019, 1, 2612−2618

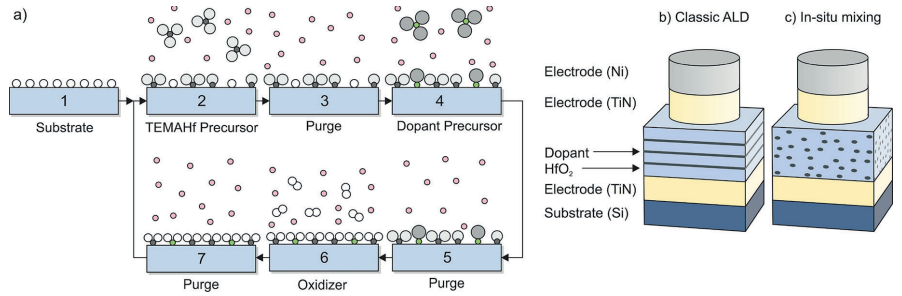

Figure 1. (a) Function principle of doping by in-situ mixing precursors. In a classical ALD process, steps four and five are not present. (b) Manufactured metal−ferroelectric−metal structures with etched top electrode (not to scale) showing the dopant distribution in a classic ALD process. (c) Enhanced dopant distribution achieved by in-situ precursor mixing.

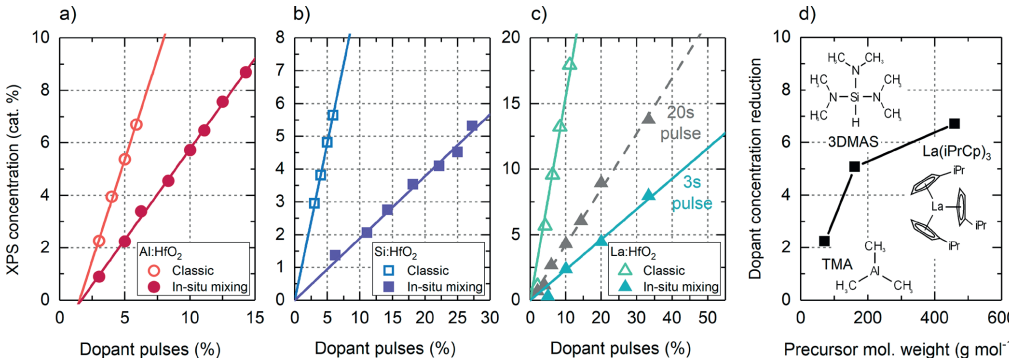

Figure 2. Dopant concentration measured via XPS vs dopant ALD pulse fraction for 10 nm thick (a) aluminum-, (b) silicon-, and (c) lanthanum-doped HfO_2. Linear scaling of the XPS measurement result vs pulse fraction is observed for all three material systems. (d) Dopant concentration ratio of classic vs precursor mixing processes calculated from the corresponding linear regressions. For comparison, the molecular weight of TEMAHf is 410 g mol^{-1}.

while another report did not find performance benefits in Al-doped HfO_2 films.[20]

■ EXPERIMENTAL SECTION

For each dopant, samples with at least four different stoichiometries are manufactured for both the classical ALD process and the in-situ precursor mixing ALD process. The layer thickness of 10 nm is confirmed by ellipsometry with a deviation of <1 nm for all samples. We employ a Jusung Eureka 3000 warm-wall reaction chamber at a process temperature of 280 °C for all samples. We employ the metal−organic precursors tetrakis(ethylmethylamido)hafnium(IV) (TEMAHf), trimethylaluminum (TMA), tris(dimethylamino)silane (3DMAS), and tris(isopropylcyclopentadienyl)lanthanum (La(iPrCp)$_3$) for HfO_2, Al_2O_3, SiO_2, and La_2O_3 deposition, respectively. Ozone is used as oxidizing agent and Ar as a purge gas. For both process variants, we use identical metal−organic precursor pulse times to allow for comparison of the results, namely 0.5 s for TMA, 2 s for 3DMAS, 3 s for La(iPrCp)$_3$, and 3 s for TEMAHf, unless noted otherwise.

To allow for electrical measurements, the samples are manufactured on strongly p-doped 300 mm Si (100) substrates. As bottom and top electrodes, we use 10 nm thick TiN deposited by ALD and chemical vapor deposition (CVD), respectively. A rapid thermal processing step is performed at 650 °C for 20 s to crystallize the films after deposition of the top electrode. For electrical measurement, nickel is deposited by E-beam evaporation using a shadow mask. An SC1 wet clean removes the exposed TiN electrode, whereby metal−ferroelectric−metal capacitors with an area of 0.1 mm^2 are defined.

For time-of-flight secondary ion mass spectroscopy (ToF-SIMS), we use samples where two 10 nm Si-doped HfO_2 layers are laminated with an ≈0.5 nm thick amorphous Al_2O_3 separator. Measurements are performed with a TOF-SIMS 300R apparatus (ION-TOF GmbH). Sputtering is achieved with 1 keV Cs ions, and 25 keV Bi ions are used for analysis in a 100 μm by 100 μm region. The stoichiometry of the samples is analyzed by X-ray photoelectron spectroscopy (XPS) using a ReVera Veraflex apparatus with Al Kα radiation at a pass energy of 141 eV. For stoichiometry uniformity analysis, we examine three positions at the wafer center, half-radius, and edge. Grazing-incidence X-ray diffraction (GI-XRD) is employed to analyze the crystallographic phase composition. We use a Bruker Discover D8 tool with Cu Kα radiation at a grazing angle of 0.5°. Rietveld refinement of GI-XRD patterns is performed using the TOPAS software package. Ferroelectric polarization−voltage ($P-U$) characteristics are obtained by using an Aixacct TF 3000 analyzer at a frequency of 1 kHz and an amplitude of 3 MV/cm. For electric field cycling, we use identical frequency and electric field settings. Switching density measurements are performed using a Keithley B2900 source measurement unit.

The precursor-mixing deposition process is depicted in Figure 1a. Initially, the TEMAHf precursor is injected and adsorbs to the surface (step 2). In the subsequent purge, the remaining TEMAHf molecules in the gas phase are removed (step 3). Now, instead of an oxidizer

DOI: 10.1021/acsaelm.9b00591
ACS Appl. Electron. Mater. 2019, 1, 2612−2618

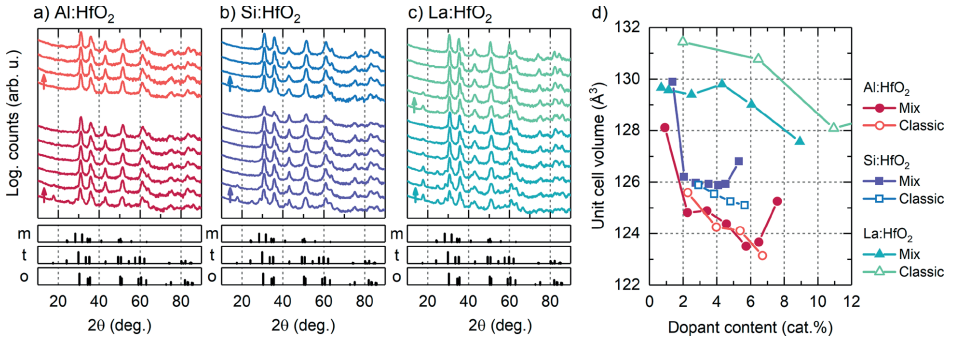

Figure 3. (a−c) GI-XRD diffractograms of 10 nm thick Al-, Si-, and La-doped HfO_2 films deposited using classic ALD nanolamination as well as in-situ precursor mixing. (d) Unit cell volume of the orthorhombic phase fraction calculated by deconvolution of the GI-XRD diffractograms.

step, the dopant precursor is injected into the process chamber, adsorbing to some of the remaining free bonding sites (step 4). Both precursor species are therefore present on the substrate surface at the same time. The ALD cycle is then completed by purging, oxidizing, and purging steps (5 to 7). By repeating steps 2 to 7, the desired film thickness is achieved.

In such a process regime, the incorporation of dopant cations is reduced with respect to the classical nanolamination technique. This is illustrated in Figures 1b and 1c, where the dopant distribution in the thin film is shown for classical ALD and in-situ precursor mixing. Because of the controlled, submonolayer growth of dopant species by precursor mixing, a uniform stoichiometry profile is achieved. In this modified process, adsorption kinetics and precursor pulse and purge timings have a particular impact on the film stoichiometry. For example, if the dopant precursor molecules experience substantial steric hindrance because of large organic ligands, the incorporation will also be low. Additionally, if the surface bond sites are already almost completely saturated after application of a long TEMAHf precursor pulse, very low dopant incorporation would be achieved. Varying the delay time after the TEMAHf pulse may also lead to desorption of some molecules, freeing up bond sites and again increasing the doping level for extended delays. This illustrates that nonideal characteristics of ALD processes have to be taken into account to achieve good results with the proposed in-situ doping process.

■ RESULTS AND DISCUSSION

X-ray photoelectron spectroscopy is performed to analyze the dopant concentration of the samples. Therefore, peak areas of Hf 4f, Al 2p, Si 2p, and La 3d are fitted by using the CasaXPS software package. In Figures 2a−c, the results for the three dopant species are summarized. For all sample groups, a linear relationship between the number of applied dopant pulses and the measured dopant concentration is observed. In the classical ALD processes, the slope of the linear regression depends on the growth per ALD cycle of the HfO_2 matrix and the dopant. For the in-situ precursor mixing processes, the slope is reduced compared to the classic processes. Thereby, the desired reduction of dopant incorporation is achieved, making concentration values of <3% accessible.

In the case of Si and La doping, the wafer-level uniformity of dopant concentration benefits from the modified process. For La-doped HfO_2, we observe relative dopant content variations of 21.4% and 4.2% throughout the 300 mm substrates for classic and in-situ mixing processes, respectively. Silicon-doped HfO_2 exhibits values of 5.5% (classic ALD) and 4.8%

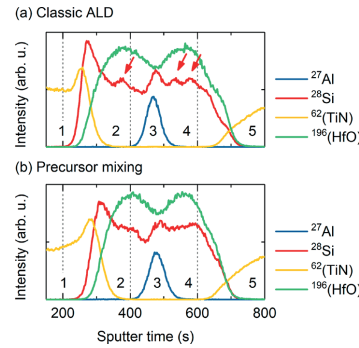

Figure 4. ToF-SIMS results with respect to sputter time for two 10 nm thick Si-doped HfO_2 layers nanolaminated with an ≈0.5 nm thick Al_2O_3 interlayer, manufactured by (a) classic ALD and (b) the proposed in-situ precursor mixing approach. Individual Si dopant peaks are visible for the film deposited by classic ALD, which are marked by arrows.

(precursor mixing). With aluminum doping, the precursor mixing approach leads to slightly reduced dopant uniformity of 5.6%, with a reference value of 3.0%. Uniformity results regarding layer thickness and doping are summarized in Table S1 of the Supporting Information. The observation of similar values around a 5% baseline for Al-, Si-, and La-doped films deposited in the in-situ mixing regime indicates that stoichiometry uniformity is dominated by the distribution of free adsorption sites. Thus, control of such vacant sites is the main pathway for uniformity tuning in the proposed process scheme. While the TMA/O_3 process already exhibits excellent uniformity in classic ALD, results indicate that in-situ precursor mixing may generally improve doping uniformity for processes with disjunct ALD process windows or otherwise challenging properties. The stability of the deposition process is analyzed by three consecutive runs of Al-doped HfO_2 with stoichiometry optimized for best ferroelectric performance. Mean film thicknesses of 9.91, 9.82, and 9.78 nm are registered for classic ALD, and 9.73, 9.81, and 9.78 nm are obtained for in-situ precursor mixing. Aluminum content measurement by XPS yielded consecutive values of 2.7, 2.5, and 2.4 cat. % for the classic approach and 2.7, 2.5, and 3.0 cat. % for the

DOI: 10.1021/acsaelm.9b00591
ACS Appl. Electron. Mater. 2019, 1, 2612−2618

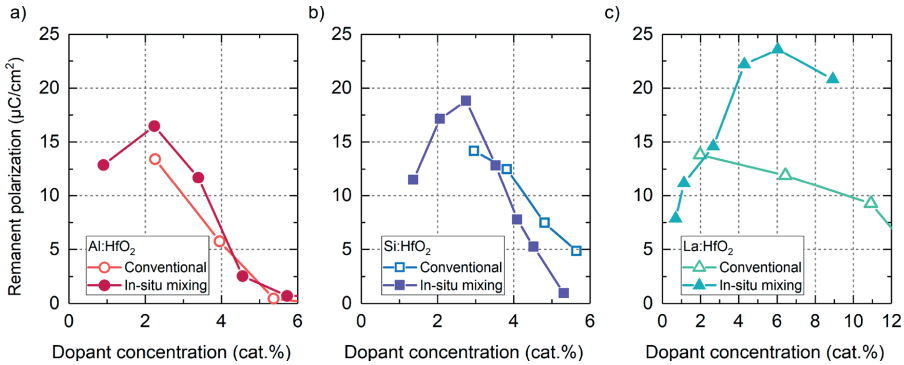

Figure 5. Remanent ferroelectric polarization of 10 nm thick (a) aluminum-, (b) silicon-, and (c) lanthanum-doped hafnium oxide thin films with respect to the dopant concentration.

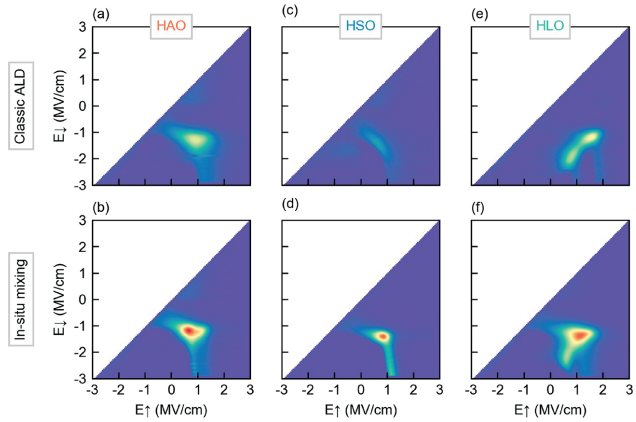

Figure 6. Preisach switching densities representing the coercive fields $E_{\uparrow}$ and $E_{\downarrow}$ of domains for (a) classic ALD with 2.3 cat. % Al doping, (b) precursor mixing with 2.2 cat. % Al doping, (c) classic ALD with 3.8 cat. % Si doping, (d) precursor mixing with 2.8 cat. % Si doping, (e) classic ALD with 6.4 cat. % La doping, and (f) precursor mixing with 6.0 cat. % La doping. All films have a thickness of 10 nm.

proposed precursor mixing. This indicates similar performance of both process regimes with respect to layer-to-layer repeatability.

We observe reduced multiplet splitting of the $3d_{5/2}$ component in La-doped HfO_2 films deposited by precursor mixing with a value of 3.86 eV compared to 4.06 eV in the classic ALD process. This is associated with reduced hydroxide and carbonate formation in the film.[21] A slightly increased C 1s peak area is observed in the precursor mixing film. However, this is close to the detection limit of our measurement setup. The La 3d fine structure splitting is equal for both processes at 16.73 and 16.72 eV, respectively. Also, the Hf 4f fine structure splitting remains constant at 1.67 eV. XPS measurement results are depicted in Figure S1 of the Supporting Information. For the Al- and Si-doped films, we could not find experimental evidence for a change in carbon or hydrogen content depending on the deposition method.

By comparing in-situ mixing and classic processes, it is possible to gain insight into the precursor adsorption during the ALD process. In Figure 2d, the quotients of slopes determined for classical and precursor-mixing processes from Figure 2a−c are depicted with respect to the precursor molecular weight. We indeed observe that for larger precursor molecules, like $La(iPrCp)_3$, the reduction of dopant incorporation is strongest with a factor of 6.7. The relatively small TMA molecules find many adsorption sites even on the TEMAHf-saturated surface, leading to a reduction factor of just 2.2.

Since self-limiting growth is an essential property of ALD, the dopant precursor pulse time is varied to study possible CVD-like reactions on the sample surface in the precursor mixing process regime. Results for Al, Si, and La dopants are shown in Figure S2a,b. For the Al-doped HfO_2 process, growth per cycle saturates quickly at 0.13 nm, which confirms that the self-terminating properties of ALD are maintained with the in-situ precursor mixing approach. Similar results, but with a lower final growth per cycle of 0.10 nm, are observed for Si doping. With La-doped HfO_2, saturation is comparably slow.

DOI: 10.1021/acsaelm.9b00591
ACS Appl. Electron. Mater. 2019, 1, 2612−2618

Both film thickness and dopant concentration continue to rise even at a pulse time of 30 s, with a decreasing slope. In the classic ALD regime, growth rates vary with values of 0.06 nm for 3DMAS/O_3, 0.10 nm for TMA/O_3, 0.10 nm for TEMAHf/O_3, and 0.21 nm for La(iPrCp)$_3$/O_3. In comparison, rather stable values of 0.10−0.13 nm per cycle are achieved by precursor mixing deposition cycles, indicating that deposition properties are dominated by the growth rate of the HfO_2 matrix. Because of the large time constant of adsorption of the La(iPrCp)$_3$ precursor, La-doped samples for electrical measurement are manufactured with a prolonged pulse time of 20 s. This sample set is depicted in Figure 2c (gray triangles), exhibiting larger La content compared to the samples with 3 s dopant precursor pulse time (solid green triangles) at similar dopant pulse ratio. We further observe TEMAHf desorption for prolonged Ar purge intervals between the TEMAHf and dopant precursor pulse. Then, the dopant incorporation rises due to the increased amount of bonding sites becoming available, which is depicted in Figure S2c.

The crystallographic structure of all manufactured films is analyzed by using GI-XRD, with results depicted in Figure 3a−c. Dissemination of the phase composition in the polycrystalline thin films is difficult due to the small crystallite size. It is further complicated by the structurally similar polymorphs of HfO_2, namely, monoclinic (m), tetragonal (t), orthorhombic (o), and cubic (c) phase fractions. As established in the literature, in lowest doped films, we observe the monoclinic peaks which are characteristic for pure HfO_2, most notably, the m-111 and m111 peaks at 28.3° and 31.7°.[22] The vicinity of the o111 and t101 peaks at 29.9° and 30.3° have been identified as helpful for understanding the formation of the polar orthorhombic phase.[6,23,24]

By use of the Rietveld refinement method,[25] the GI-XRD diffractograms are deconvoluted, where diffraction data of monoclinic,[22] tetragonal,[23] and orthorhombic[24] phase fractions, as well as TiN electrodes,[26] are included. Weighted-profile *R*-factors are used to quantify agreement between refinement results and experimental data. Values of 14−17 (Al:HfO_2), 10−14 (Si:HfO_2), and 15−19 (La:HfO_2) are obtained, which is comparable to other reports on phase analysis of doped HfO_2 with similar instrumentation.[27,28] Calculated unit cell volumes for the orthorhombic $Pca2_1$ phase are shown in Figure 3d with respect to the dopant content. As expected, the unit cell volume depends on the dopant species: Al-doped HfO_2 exhibits the smallest unit cell with 123−128 Å^3, followed by Si:HfO_2 with a volume of 125−130 Å^3. Even though Si has a smaller ionic radius of 54 pm compared to Al at 68 pm,[29] the tetravalence of Si may cause the observation of a larger unit cell. The La-doped HfO_2 films reach the largest unit cell volumes at 128−132 Å^3 at an ionic radius of 117 pm for La^{3+}. It is somewhat surprising that the unit cell volume reduces for increasing La doping, as the ionic radius of Hf^{4+} at 85 pm is smaller than that of La^{3+}. Doped hafnium oxide thin films are considered to be composed of a phase mixture of the mentioned polymorphs. The reduction of unit cell volume for all three dopant species indicates a common cause of this trend, namely, the transformation of monoclinic grains to polar orthorhombic and then ultimately tetragonal or cubic fractions with increasing dopant content, which has also been observed in other studies.[27] This explanation is supported by theoretical investigations,[2] where m-HfO_2 exhibits a large unit cell volume of 138 Å^3, the ferroelectric polar phase a reduced value of 134 Å^3, and t-HfO_2, and c-HfO_2 further decreased values of 131 and 128 Å^3, respectively. While there is a slight deviation in the absolute values, the trend suggests a common phase evolution of all three examined material systems. The increasing unit cell volume for the highest doped Al:HfO_2 and Si:HfO_2 layers is explained by an increased crystallization temperature, which leads to partially amorphous films.

When comparing unit cell volumes of dopant mixing and classic ALD processes, Al:HfO_2 shows almost no difference (red circles), and unit cell volumes for Si:HfO_2 differ only for higher dopant concentrations (blue squares). The difference is pronounced for La:HfO_2, where the classic process (open triangles) shows a much higher unit cell volume compared to the in-situ doping process (filled triangles), which is attributed to a higher defect density in the classic ALD process.

Direct observation of dopant distribution in the depth of the HfO_2 films is challenging, as high spatial resolution and large element sensitivity are needed. ToF-SIMS achieves this by successive sputtering of the sample alternating with element analysis via mass spectroscopy. However, it is noted that the method yields only qualitative composition information. In films with a thickness of 10 nm, we observe that the minute variations in dopant concentration are concealed by interface effects. These arise from charge buildup at the metal−ferroelectric interface by ion bombardment.[30] Additionally, variations of the sputter rate in regions of high defect density can lead to artifacts. Thus, nanolaminates of two 10 nm Si-doped HfO_2 layers separated by ≈0.5 nm thick Al_2O_3 are analyzed, which are similar to films discussed in an earlier work.[12] Results are depicted in Figure 4a, with signals for ^{27}Al (blue), the dopant ^{28}Si (red), ^{62}(TiN) (yellow), and ^{196}(HfO) (green). The different regions of the film stack are clearly visible, namely top electrode (1), the first Si-doped HfO_2 layer (2), Al_2O_3 interlayer (3), the second doped HfO_2 layer (4), and finally the bottom electrode (5). The ^{28}Si signal exhibits characteristic maxima (red arrows), which correspond to the individual SiO_2 deposition cycles in the classic ALD scheme. In Figure 4b, results for the in-situ precursor mixing approach are shown, where the ^{28}Si signal exhibits a flatter shape, indicating improved distribution of the dopant cations in the HfO_2 matrix.

While the results of XPS and XRD analysis hint on a link between the uniform distribution of dopants within the ferroelectric thin films and enhancement of film quality, electrical measurements will provide clarity how the ferroelectric behavior is impacted by the different process variants. In Figure 5a−c, the remanent polarization P_r extracted from polarization−voltage measurements is depicted for Al-, Si-, and La-doping, respectively. All samples are field cycled 10^5 times beforehand. The corresponding $P-U$ characteristics are shown in Figure S3. For all three dopants, the largest remanent polarization is reached with the in-situ precursor mixing process. The maximum P_r values are 16.5 μC/cm^2 for Al, 18.8 μC/cm^2 for Si, and 23.6 μC/cm^2 for La doping. For the in-situ precursor mixing process, P_r exhibits a peak at a certain dopant concentration, which is expected as neither pure HfO_2 nor the dopant oxides are ferroelectric on their own. We find optimal stoichiometries of 2.2 cat. % for Al, 2.7 cat. % for Si, and 6.0 cat. % for La doping, which is similar to published values.[6,28,31] When comparing both ALD process variants, the enhancement of remanent polarization is most pronounced for La doping and smallest for Al-doped HfO_2. The results show that the precursor mixing process allows for stoichiometry

DOI: 10.1021/acsaelm.9b00591
ACS Appl. Electron. Mater. 2019, 1, 2612−2618

optimization in a wide range while achieving superior electrical performance compared to classic thermal ALD.

To investigate causes of the P_r difference of both process variants, we perform first-order reversal curve measurements.[16] From the measurement results, we obtain the switching density of the film with respect to the positive and negative coercive fields $E_\uparrow$ and $E_\downarrow$ of the individual domains. Experimental results are depicted in Figure 6a−f, where all samples are field cycled 10^4 times beforehand to reduce wake-up effects. When comparing the switching densities of both process variants, it is evident that in-situ precursor mixing yields more confined switching peaks with larger intensity. The films deposited using classic ALD also show undesirable antiferroelectric-like split peak contributions (Si-doped HfO_2 and La-doped HfO_2). The coercive field of ≈±1 MV/cm in the Preisach density matches the value extracted from the $P-U$ measurement.

CONCLUSIONS

We demonstrate that in-situ precursor mixing can substantially enhance the ferroelectric properties of doped hafnium oxide thin films in thermal ALD processes. By using precursor mixing, we can precisely optimize the stoichiometry for three dopant species: aluminum, silicon, and lanthanum. The proposed ALD process reduces the incorporation of dopant species into the HfO_2 matrix, thus making low dopant contents accessible while maintaining uniform stoichiometry throughout the film. We observe distinct ferroelectric switching with no antiferroelectric-like contributions and P_r values of 16.5 $\mu C/cm^2$ for Al:HfO_2, 18.8 $\mu C/cm^2$ for Si:HfO_2, and 23.6 $\mu C/cm^2$ for La:HfO_2. The prescribed in-situ precursor mixing process may be adapted to future large-scale manufacturing processes by mixing the precursors beforehand, which requires knowledge on possible chemical interactions.

ASSOCIATED CONTENT

Supporting Information

The Supporting Information is available free of charge at https://pubs.acs.org/doi/10.1021/acsaelm.9b00591.

Uniformity of thickness, stoichiometry, and ferroelectric remanent polarization; XPS measurement results of 10 nm La-doped HfO_2 films; growth per ALD cycle of all demonstrated processes with respect to precursor pulse timing; TEMAHf precursor desorption characteristics; polarization−voltage hysteresis graphs for Al-, Si-, and La-doped HfO_2 (PDF)

AUTHOR INFORMATION

Corresponding Author

*E-mail: clemens.mart@ipms.fraunhofer.de.

ORCID

Clemens Mart: 0000-0002-1828-2187

Notes

The authors declare no competing financial interest.

ACKNOWLEDGMENTS

This work was funded via subcontract from Globalfoundries Dresden Module One within the framework Important Project of Common European Interest (IPCEI) by the Federal Ministry for Economics and Energy and by the State of Saxony. Alireza M. Kia is acknowledged for providing ToF-SIMS measurements.

REFERENCES

(1) Böscke, T. S.; Müller, J.; Bräuhaus, D.; Schröder, U.; Böttger, U. Ferroelectricity in hafnium oxide thin films. *Appl. Phys. Lett.* **2011**, *99*, 102903.

(2) Materlik, R.; Künneth, C.; Kersch, A. The origin of ferroelectricity in $Hf_{1-x}Zr_xO_2$: A computational investigation and a surface energy model. *J. Appl. Phys.* **2015**, *117*, 134109.

(3) Shiraishi, T.; Katayama, K.; Yokouchi, T.; Shimizu, T.; Oikawa, T.; Sakata, O.; Uchida, H.; Imai, Y.; Kiguchi, T.; Konno, T. J.; Funakubo, H. Impact of mechanical stress on ferroelectricity in (Hf 0.5 Zr 0.5)O 2 thin films. *Appl. Phys. Lett.* **2016**, *108*, 262904.

(4) Hoffmann, M.; Schroeder, U.; Schenk, T.; Shimizu, T.; Funakubo, H.; Sakata, O.; Pohl, D.; Drescher, M.; Adelmann, C.; Materlik, R.; Kersch, A.; Mikolajick, T. Stabilizing the ferroelectric phase in doped hafnium oxide. *J. Appl. Phys.* **2015**, *118*, 072006.

(5) Lee, T. Y.; Lee, K.; Lim, H. H.; Song, M. S.; Yang, S. M.; Yoo, H. K.; Suh, D. I.; Zhu, Z.; Yoon, A.; MacDonald, M. R.; Lei, X.; Jeong, H. Y.; Lee, D.; Park, K.; Park, J.; Chae, S. C. Ferroelectric Polarization-Switching Dynamics and Wake-Up Effect in Si-Doped HfO_2. *ACS Appl. Mater. Interfaces* **2019**, *11*, 3142−3149.

(6) Park, M. H.; Lee, Y. H.; Kim, H. J.; Kim, Y. J.; Moon, T.; Kim, K. D.; Müller, J.; Kersch, A.; Schroeder, U.; Mikolajick, T.; Hwang, C. S. Ferroelectricity and antiferroelectricity of doped thin HfO2-based films. *Adv. Mater. (Weinheim, Ger.)* **2015**, *27*, 1811−1831.

(7) Riedel, S.; Polakowski, P.; Müller, J. A thermally robust and thickness independent ferroelectric phase in laminated hafnium zirconium oxide. *AIP Adv.* **2016**, *6*, 095123.

(8) Xu, L.; Nishimura, T.; Shibayama, S.; Yajima, T.; Migita, S.; Toriumi, A. Kinetic pathway of the ferroelectric phase formation in doped HfO_2 films. *J. Appl. Phys.* **2017**, *122*, 124104.

(9) Mueller, S.; Mueller, J.; Singh, A.; Riedel, S.; Sundqvist, J.; Schroeder, U.; Mikolajick, T. Incipient Ferroelectricity in Al-Doped HfO_2 Thin Films. *Adv. Funct. Mater.* **2012**, *22*, 2412−2417.

(10) Ali, T.; Polakowski, P.; Riedel, S.; Büttner, T.; Kämpfe, T.; Rudolph, M.; Pätzold, B.; Seidel, K.; Löhr, D.; Hoffmann, R.; Czernohorsky, M.; Kühnel, K.; Thrun, X.; Hanisch, N.; Steinke, P.; Calvo, J.; Müller, J. Silicon doped hafnium oxide (HSO) and hafnium zirconium oxide (HZO) based FeFET: A material relation to device physics. *Appl. Phys. Lett.* **2018**, *112*, 222903.

(11) Kühnel, K.; Czernohorsky, M.; Mart, C.; Weinreich, W. High-density energy storage in Si-doped hafnium oxide thin films on area-enhanced substrates. *J. Vac. Sci. Technol., B: Nanotechnol. Microelectron.: Mater., Process., Meas., Phenom.* **2019**, *37*, 021401.

(12) Mart, C.; Kämpfe, T.; Zybell, S.; Weinreich, W. Layer thickness scaling and wake-up effect of pyroelectric response in Si-doped HfO_2. *Appl. Phys. Lett.* **2018**, *112*, 052905.

(13) Mulaosmanovic, H.; Ocker, J.; Muller, S.; Noack, M.; Muller, J.; Polakowski, P.; Mikolajick, T.; Slesazeck, S. Novel ferroelectric FET based synapse for neuromorphic systems. In *2017 Symposium on VLSI Technology*; IEEE: 2017; pp T176−T177.

(14) Lomenzo, P. D.; Takmeel, Q.; Zhou, C.; Liu, Y.; Fancher, C. M.; Jones, J. L.; Moghaddam, S.; Nishida, T. The effects of layering in ferroelectric Si-doped HfO_2 thin films. *Appl. Phys. Lett.* **2014**, *105*, 072906.

(15) Umezawa, N.; Shiraishi, K.; Sugino, S.; Tachibana, A.; Ohmori, K.; Kakushima, K.; Iwai, H.; Chikyow, T.; Ohno, T.; Nara, Y.; Yamada, K. Suppression of oxygen vacancy formation in Hf-based high-k dielectrics by lanthanum incorporation. *Appl. Phys. Lett.* **2007**, *91*, 132904.

(16) Schenk, T.; Hoffmann, M.; Ocker, J.; Pešić, M.; Mikolajick, T.; Schroeder, U. Complex Internal Bias Fields in Ferroelectric Hafnium Oxide. *ACS Appl. Mater. Interfaces* **2015**, *7*, 20224−20233.

(17) Mart, C.; Kühnel, K.; Kämpfe, T.; Zybell, S.; Weinreich, W. Ferroelectric and pyroelectric properties of polycrystalline La-doped HfO_2 thin films. *Appl. Phys. Lett.* **2019**, *114*, 102903.

(18) Chouprik, A.; Spiridonov, M.; Zarubin, S.; Kirtaev, R.; Mikheev, V.; Lebedinskii, Y.; Zakharchenko, S.; Negrov, D. Wake-Up in a $Hf_{0.5}Zr_{0.5}O_2$ Film: A Cycle-by-Cycle Emergence of the Remnant Polarization via the Domain Depinning and the Vanishing

DOI: 10.1021/acsaelm.9b00591
ACS Appl. Electron. Mater. 2019, 1, 2612−2618

of the Anomalous Polarization Switching. *ACS Appl. Electron. Mater.* **2019**, *1*, 275−287.
(19) Bönhardt, S.; Kühnel, K.; Kia, A. M.; Weinreich, W. Formation of highly conformal spinel lithium titanate thin films based on a novel three-step atomic layer deposition process. *J. Vac. Sci. Technol., A* **2019**, *37*, 031508.
(20) Vulpe, S.; Nastase, F.; Dragoman, M.; Dinescu, A.; Romanitan, C.; Iftimie, S.; Moldovan, A.; Apostol, N. Physical properties of the ferroelectric capacitors based on Al-doped HfO_2 grown via Atomic Layer Deposition on Si. *Appl. Surf. Sci.* **2019**, *483*, 324−333.
(21) *Handbook of X-ray Photoelectron Spectroscopy: A Reference Book of Standard Spectra for Identification and Interpretation of XPS Data*; Moulder, J. F., Chastain, J., Eds.; Update; Perkin-Elmer Corporation: Eden Prairie, MN, 1992.
(22) International Centre for Diffraction Data. PDF Card No. 00-034-0104: PDF-4+ 2019, Newtown Square, PA, 2018.
(23) International Centre for Diffraction Data. PDF Card No. 04-011-8820: PDF-4+ 2019, Newtown Square, PA, 2018.
(24) International Centre for Diffraction Data. PDF Card No. 04-005-5597: PDF-4+ 2019, Newtown Square, PA, 2018.
(25) Rietveld, H. M. Line profiles of neutron powder-diffraction peaks for structure refinement. *Acta Crystallogr.* **1967**, *22*, 151−152.
(26) International Centre for Diffraction Data. PDF Card No. 00-038-1420: PDF-4+ 2019, Newtown Square, PA, 2018.
(27) Park, M. H.; Schenk, T.; Fancher, C. M.; Grimley, E. D.; Zhou, C.; Richter, C.; LeBeau, J. M.; Jones, J. L.; Mikolajick, T.; Schroeder, U. A comprehensive study on the structural evolution of HfO 2 thin films doped with various dopants. *J. Mater. Chem. C* **2017**, *5*, 4677−4690.
(28) Schroeder, U.; Richter, C.; Park, M. H.; Schenk, T.; Pešić, M.; Hoffmann, M.; Fengler, F. P. G.; Pohl, D.; Rellinghaus, B.; Zhou, C.; Chung, C.-C.; Jones, J. L.; Mikolajick, T. Lanthanum-Doped Hafnium Oxide: A Robust Ferroelectric Material. *Inorg. Chem.* **2018**, *57*, 2752−2765.
(29) Shannon, R. D. Revised effective ionic radii and systematic studies of interatomic distances in halides and chalcogenides. *Acta Crystallogr., Sect. A: Cryst. Phys., Diffr., Theor. Gen. Crystallogr.* **1976**, *32*, 751−767.
(30) Stevie, F. A. *Secondary Ion Mass Spectrometry: Applications for Depth Profiling and Surface Characterization*; Materials characterization and analysis collection; Momentum Press: New York, 2016.
(31) Muller, J.; Boscke, T. S.; Muller, S.; Yurchuk, E.; Polakowski, P.; Paul, J.; Martin, D.; Schenk, T.; Khullar, K.; Kersch, A.; Weinreich, W.; Riedel, S.; Seidel, K.; Kumar, A.; Arruda, T. M.; Kalinin, S. V.; Schlosser, T.; Boschke, R.; van Bentum, R.; Schroder, U.; Mikolajick, T. Ferroelectric hafnium oxide: A CMOS-compatible and highly scalable approach to future ferroelectric memories. In *2013 IEEE International Electron Devices Meeting*; IEEE: 2013; pp 10.8.1−10.8.4.

DOI: 10.1021/acsaelm.9b00591
ACS Appl. Electron. Mater. 2019, 1, 2612−2618

2

STRUCTURAL PROPERTIES

In this chapter the structural properties resulting in ferroelectricity and the implications of polycrystallinity of the HfO_2 films onto its electrical behavior, e.g. electrical cycling, will be discussed.

2.1 FERROELECTRICITY AS A STRUCTURAL PROPERTY

Ferroelectricity can be treated as a phase transition with an intrinsic loss in symmetry. The conventional theory to describe such a process has been developed by Ginzburg and Landau. Hereby, the crystal state is described by a set of parameters such as temperature T, entropy S, electrical field strength $\vec{E}$, polarization $\vec{P}$, stress σ or strain ε in thermodynamic equilibrium. The free energy of the crystal system can be expressed as a power series of the polarization $\vec{P}$: [52]

$$F(\vec{P}, T, \vec{E}) = -\vec{E} \cdot \vec{P} + \frac{1}{2}a\vec{P}^2 + \frac{1}{4}b\vec{P}^4 + \frac{1}{6}c\vec{P}^6 + \dots \tag{1}$$

with $a = \gamma(T - T_C)$, T_C the Curie temperature of the ferroelectric phase transition, $\vec{P}_S$ the spontaneous polarization and $a, b, c, \dots$ the so-called ferroelectric coefficients. F is depicted in Fig. 2a for a uniaxial ferroelectric at different temperatures. For temperatures below T_C the free-energy being expressed up to forth order[1], results in two local minima, resulting in a spontaneous and remanent non-zero polarization. Above T_C, one observes the minimal free-energy for a zero polarization. Therefore, T_C resembles the transition temperature between the ferroelectric and paraelectric phases.

A prototype material is BTO, which has six free energy minima at room temperature. The associated ferroelectric polarization states are either parallel or perpendicular to the crystallographic axis. Upon the application of an external electric field exceeding the coercive field $\vec{E}_C$, the polarization can flip. For the discussed idealized and especially uniaxial ferroelectric, the hysteresis loop of $\vec{E}$ vs. $\vec{P}$ is given in Fig. 2b. In the case of $b > 0$, there is a second-order phase transition at $T = T_C$. The temperature-dependence of the spontaneous polarization P_S can be expressed in this case by

$$\vec{P}_S = \vec{P}_0 \sqrt{a/b(T_C - T)} \qquad \text{for} \quad T < T_C, \tag{2}$$

1 One typically designates such potentials as Mexican hat potentials.

which is illustrated in Fig. 2c. The electrical susceptibility $\chi = \partial\vec{P}/\partial\vec{E}|_{\vec{P}_o}$ shows a singularity at T_C as can be seen in Fig. 2d.

It is useful to approach the topic of ferroelectricity in terms of crystallography [see Fig. 3]. Crystals can be divided into 32 point groups[2], of which 11 show centrosymmetric and 21 non-centrosymmetric behavior. Among the non-centrosymmetric point groups 20 reveal piezoelectricity.

While piezoelectric crystals lack inversion symmetry, they do not necessarily possess a unique polar axis and, therefore, stable electric dipoles. Of the 20 point groups permitting piezoelectricity, only 10 support an electrical dipole moment in the unstrained state. This permanent dipole is often referred to as the spontaneous polarization P_S. Crystals of one of these 10 point groups will have charges that change as the material's temperature is uniformly altered. Crystals possessing this property are classified as pyroelectrics.

Ferroelectricity is defined as a crystal property where a permanent dipole can be reoriented upon an electric field. Because ferroelectric crystals must have a permanent dipole, they are also pyroelectric and must possess crystal symmetry belonging to one of the 10 pyroelectric groups. The distinguishing characteristic of a ferroelectric crystal from all other pyroelectric crystals is the reorientabilty of the dipole moment. For example, AlN is a pyroelectric material, but under the application of an electric field opposing the dipole direction, it will undergo dielectric breakdown prior to the switching of the polarization to the opposite direction. On the other hand, e.g. $LiNbO_3$ is also pyroelectric, but the polarization direction can be switched by 180° upon electric field. Hereby, the crystal will generate a polarization $\vec{P}$ upon external strain σ.

10 of the latter point groups give rise to pyroelectricity, which is in the case of ferroelectric materials connected with the temperature-dependent remanent polarization of it. Hence, ferroelectric HfO_2 thin films are especially expected to also show piezoelectric and pyroelectric behavior.

Ferroelectric materials retain their polarization P even under absence of an external field E_{ext}, which is why it is as well defined by the existence of a spontaneous polarization P_S. In general, the polarization is induced by a lattice distortion, resulting in an ion displacement. Thus, separated charged centers are created, forming a unit cell electric dipole

$$\vec{p} = q \cdot \vec{l}/V \tag{3}$$

with the separated charge q, the displacement $\vec{l}$ and unit cell volume V.

2 A point group is a set of geometric symmetries (isometries), such as mirroring or rotation, that keep at least one point fixed. The crystal lattice can fulfill these symmetries.

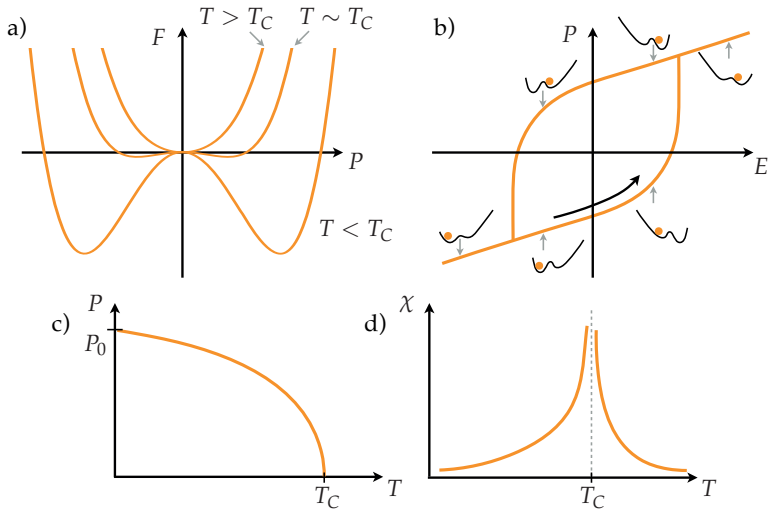

Figure 2: Landau theory of uni-axial ferroelectrics; a) free energy F as a function of polarization P for different temperatures T below, at or above T_C, retrieving two definite local minima for $T < T_C$ for an uniaxial ferroelectric, b) schematic of the hysteresis loop upon application of an external electric field E and depicting the free-energy and polarization configurations for the different external electric field configurations for an ideal ferroelectric, c) temperature dependence of the spontaneous polarization P_S for $b > 0$, resulting in a second-order phase transition at $T = T_C$, d) associated susceptibility $\chi = \partial P/\partial E|_{P_o}$.

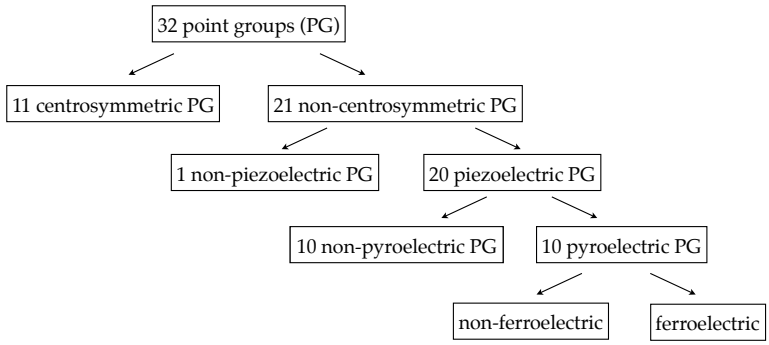

Figure 3: Crystallographic analysis of the point groups (PG) with different properties like centrosymmetry, piezoelectricity, pyroelectricity and ferroelectricity, inspired by [53].

Various crystallographic phases were known for bulk HfO_2 such as monoclinic, tetragonal and cubic [54]. The monoclinic phase has been known to be the room-temperature stable ground state for bulk systems. However, for thin films further influences such as film stress, thermal quenching, interface formation, polycrystallinity etc. resulting in polymorphic films were expected to have an influence on the scaling of nanoelectronic devices. Hence, due to this polymorphism, an amorphous film was targeted, e.g. by additional doping by silicon, to result in better film homogeneity. However, for larger film thicknesses, which still resembles an ultra-thin film, such as 10 nm, a butterfly curve in the capacitance-voltage curve was observed indicating the appearance of ferroelectricity in the crystallized film after rapid thermal annealing [5]. This finding revealed scepticism as all known bulk stable crystallographic phases, the monoclinic ($P2_1/c$), tetragonal ($P4_2/mmc$) and cubic ($Fm\bar{3}m$) phase, are all centrosymmetric and would hence not give rise to ferroelectricity. Afterwards, further studies confirmed the existence of the ferroelectricity in HfO_2 thin films, which revealed the by-then first CMOS-compatible ferroelectric material. We now believe, based on ab-initio theoretical analysis as well as electron diffraction measurements [55], that mainly the polar and thus non-centrosymmetric orthorhombic phase ($Pca2_1$) is contributing to the discussed ferroelectricity.

So far, the polarization in the ferroelectric material was treated as entirely uniform and spatially infinite, which is far from the real case. In a realistic ferroelectric system, domains (regions of common polarization orientation) and, for the case of a poly-crystalline film, grains (compartments of common crystallographic orientation) are formed.

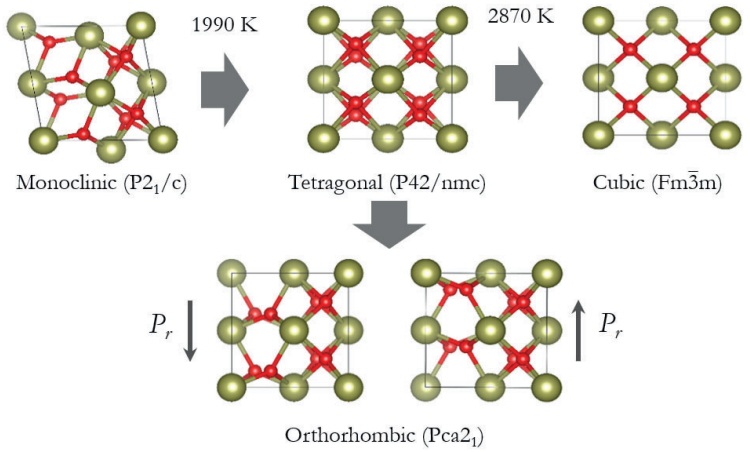

Figure 4: Crystallographic single cells of HfO_2 as derived from ab-initio simulations, including the ground-state (monoclinic, P2$_2$/c) and high-temperature phases (tetragonal, P42/nm; cubic, Fm$\bar{3}$m) as well as the generally considered metastable ferroelectric phase (polar orthorhombic, Pca2$_1$) in two polarisation states.

For the existence of domains several reasons exist, such as the introduction of non-uniform strain, emergence of microscopic defects, and the thermal and electrical cycling of the sample. But even in an ideal single crystal, domains are to be expected for energetic reasons associated with electrostatics under absence of screening. Single-domain states are commonly unfavorable due to the necessary depolarization energy at the crystal surface which are caused by the electrostatic field. The resulting electrostatic energy can be minimized by the formation of different, e.g opposing, domains. These domains are separated by a domain wall. The formation of domain walls requires an additional energy, hence, a certain domain size will correspond to the energy minimum. In a model introduced by Kittel [56] the domain width w was shown to depend on the material thickness d in the way that w^2/d equals a constant c.

Typically, domain walls have been observed depending on the crystallographic point group of the material such as 180°, 90°, 72°, etc. Hereby, the angle denotes the change in crystal axis from one to the other domain. For HfO_2, it was found that, contrary to conventional ferroelectrics with spread dipoles, we can observe flat phonon bands with little crystal distortion, e.g. close to domain walls, resulting in domain walls at zero-size and making it individually switchable per unit cell without creating any domain-wall energy cost [58], see Fig. 5. This has also been

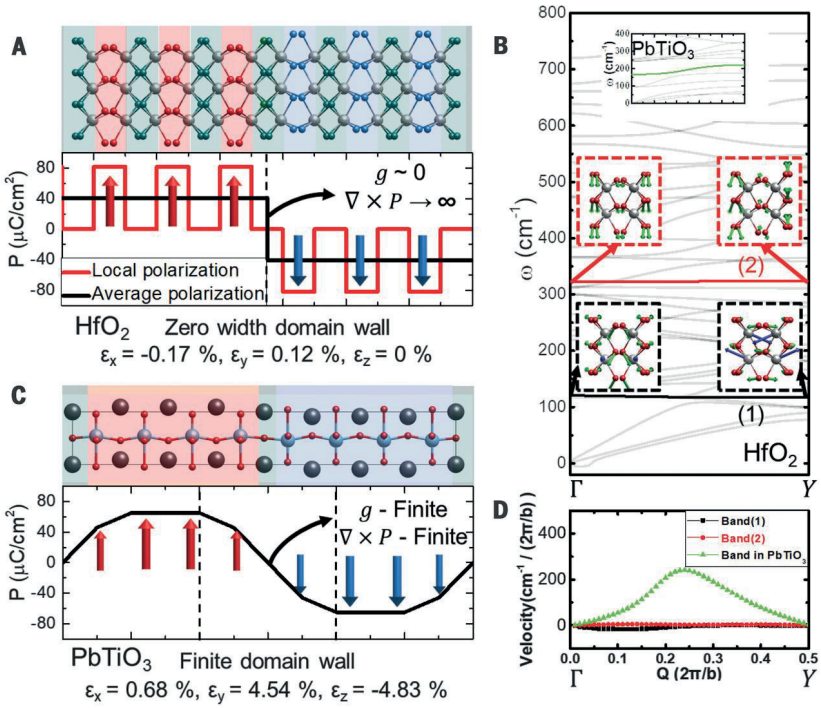

Figure 5: Flat bands and zero-width domain wall in HfO_2, contrary to the diffused domain wall in $PbTiO_3$ (a) and (c). Hereby, the red and black lines denote the local polarization averaged over their half– and single–unit cells, respectively. $\nabla \times P$ is singularly large and highly localized at the domain wall in HfO_2. Flat polar bands are indicated with black and red lines, and eigenmodes at Γ and Y in the bands are depicted in the insets. The flatness of the bands in HfO_2 is in sharp contrast to a dispersive band in $PbTiO_3$ ((b), top, inset). (d) Phonon velocities of the flat bands in HfO_2 are nearly zero. Reprinted with permission from [57] .

supported by research on the domain wall energy barrier in HfO_2, which can be reduced to ca. 3 % according to a recent DFT analysis [57].

In both analyses only 180° domain walls were considered. However, also 90° domain walls can be found, which are also called ferroelastic domain walls, due to the internal strain they require connected to the non-cubic unit cell.

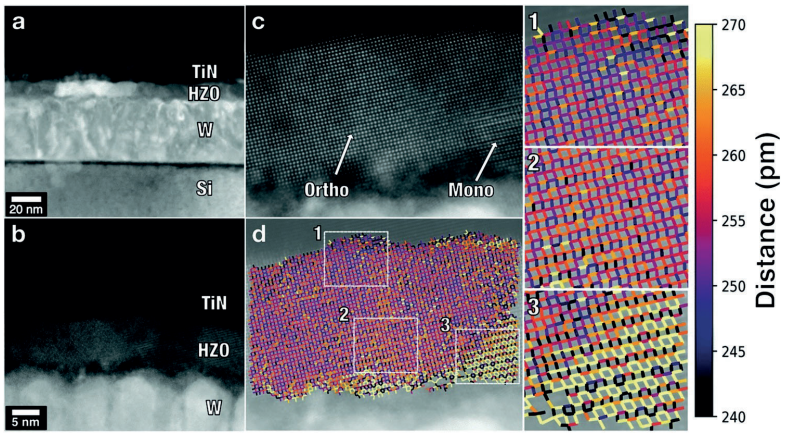

Figure 6: TEM and HAADF TEM image of a HZO film, featuring domains inside that film within a single grain, particularly a 90° domain wall. Reproduced with permission from [55].

2.2 TEXTURE ANALYSIS ON TITANIUM NITRIDE SUBSTRATE

Only very scarce direct experimental observation of domain walls have been presented in HfO_2 so far, e.g using piezo-response force microscopy (PFM)[3] and high-resolution transmission electron microscopy (HRTEM). 90° domain walls have been observed in HRTEM with domain sizes below 10 nm, see Fig. 6. Besides HRTEM and PFM, a new technique was developed, which can reveal the crystallographic orientation and phase of the commonly available polycrystalline films of HfO_2, which will be discussed and used in the next sections.

As previously discussed, upon anneal of the amorphous hafnium oxide layer, a polycrstalline film is formed. This crystallization process is the essential step in the formation of the crystallites with a polar crystal structure. In Fig. 7 the dynamics upon cool-down are shown, revealing a clear transition from the high-temperature

3 PFM intrinsically has low spatial resolution in investigating the nature of ferroelectric domain walls in HfO_2.

phases to the metastable orthorhombic phase at around 800 °C for various doping atom film configurations such as Al, Gd, Sc.

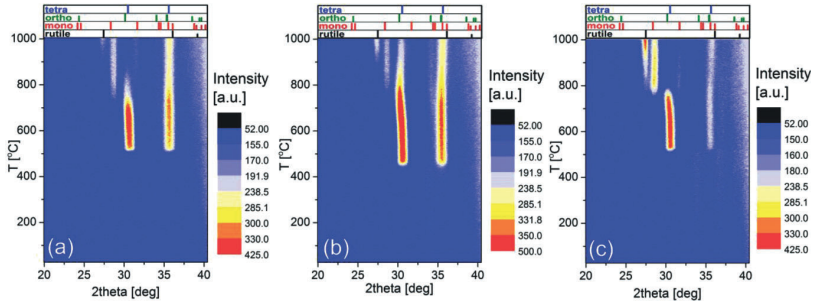

Figure 7: Crystallization dynamics in ultra-thin hafnium oxide films recorded by X-ray diffraction (XRD) for 10 nm thick a) Al-, b) Gd-, and c) Sr-doped HfO_2 thin films with reference tick marks ($P4_2/nmc$ tetragonal, $Pca2_1$ orthorhombic, $P2_1/c$ monoclinic phases of HfO_2 and P42/mmm rutile phase of TiO_2) in the upper panels. Reprinted with permission from [59].

Besides texture, which is a variation of the orientation of the grains within the film, also various phase compositions are possible in such a polymorphic and polycrystalline film. However, early works in the study of the crystallographic composition of these layers was not permitted with the commonly applied techniques such as GIXRD. It did not allow to obtain a visualization of these grains as well as it only allowed the analysis of the composition of these phases with very limited scope, as the ratio of monoclinic vs. higher symmetric phases was investigated in such films for instance [42].

Here, the local crystallographic orientation of these grains constituting the polycrystalline film has been studied. Hereby, a novel technique was used, referred to as transmission Kikuchi diffraction (TKD) [60], which is an optimization of the transmission-type electron back-scattered diffraction (EBSD). It enables a high lateral resolution of the electron beam diffraction upon scanning the beam over the sample [61]. Upon transformation of the diffraction pattern into the Hough space, it is possible to extract both the crystallographic phase and the orientation of the grains as well as their shape upon scan.

As discussed, various crystallographic phases can be expected in HfO_2 from ab-initio investigation. Some of these phases possess a non-centrosymmetric structure with the polar orthorhombic phase generally considered to be the source of ferroelectricity in HfO_2 films [63]. However, further polar phases such as a polar

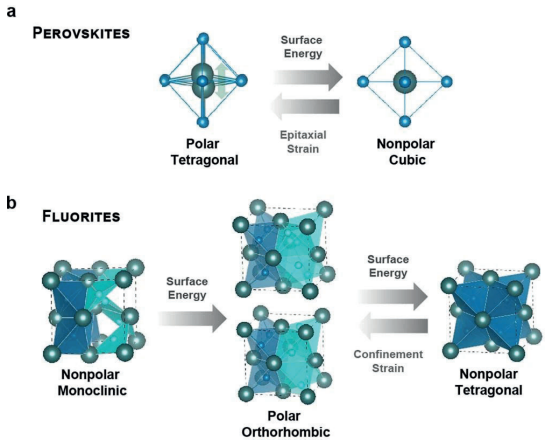

Figure 8: Strain influences on formation of ferroelectric phases in perovskites and fluorites such as hafnium oxide. Reprinted with permission: [62].

rhombohedral phase have been reported upon epitaxial growth conditions as well [64]. Besides the polar orthorhombic phase of space group $Pca2_1$, two other orthorhombic phases, with the space group Pbca and Pnma, respectively, have been reported in the literature [65]. These two phases are stabilized by high pressure, but they do have an inversion center which would not allow the emergence of ferroelectricity.

In the referenced publication, we investigated the local orientation and phases of the grains by using TKD in one conventional device configuration as integrated on top of the electrode material titanium nitride (TiN) [61]. The TKD technique was applied onto a HZO thin film. The samples were dimple-grindered. The TKD measurement was performed in a scanning electron microscope (SEM) with the dedicated TKD detector Optimus by Bruker. Hereby, the electron beam incident perpendicular to the sample surface, with the detector placed below the sample. The electron diffraction pattern with the Kikuchi pattern is imaged, which dependent on the local crystallographic properties such as phase and orientation.

The recorded Kikuchi patterns can be analyzed with the crystallographic parameters of the different known phases as well as ab-initio-generated crystal parameters. It could be shown that the monoclinic phase is only present in a small fraction and only in relatively large grains, whereas the ferroelectric orthorhombic phase is present in the full range of grain sizes. Furthermore, an out-of-plane texture of the [010]-axis was found in the polycrystalline film, which is visible in the

inverse pole figure along the z-axis (IPFz), which can be explained by persistent tensile strain during the annealing step. This explains the very good ferroelectric properties extracted for this ferroelectric thin film capacitors.

Furthermore, the technique makes it possible to visualize the intra-granular misorientation or stress within the grains. That is important in understanding the crystallization process of the thin film as well as understand stress-related influences to the wake-up effect (cp. Sec. 2.5). An extension of this technique can also be applied on previously integrated ferroelectric capacitors as will be discussed in Sec. 2.4, e.g. MFM capacitors [66]. Besides TKD we have also used the combination of Rietveld refinement method on GIXRD with a fit analysis on grazing incidence EXAFS to extract quantitative phase fractions, matching the TKD results [67].

PUBLICATION: Local crystallographic phase detection and texture mapping in ferroelectric Zr doped HfO_2 films by transmission-EBSD

PUBLICATION DETAILS The following publication is reproduced with permission from: M. Lederer, T. Kämpfe, R. Olivo, D. Lehninger, C. Mart, S. Kirbach, T. Ali, P. Polakowski, L. Roy, and K. Seidel, "Local crystallographic phase detection and texture mapping in ferroelectric Zr doped HfO_2 films by transmission-EBSD", Applied Physics Letters 115, 22902, (2019). Selected as Editor's Pick. Copyright 2019 American Physical Society.

Applied Physics Letters ARTICLE scitation.org/journal/apl

Local crystallographic phase detection and texture mapping in ferroelectric Zr doped HfO_2 films by transmission-EBSD

Cite as: Appl. Phys. Lett. **115**, 222902 (2019); doi: 10.1063/1.5129318
Submitted: 27 September 2019 · Accepted: 11 November 2019 ·
Published Online: 27 November 2019

View Online Export Citation CrossMark

M. Lederer,[a] T. Kämpfe, R. Olivo, D. Lehninger, C. Mart, S. Kirbach, T. Ali, P. Polakowski, L. Roy, and K. Seidel

AFFILIATIONS

Fraunhofer IPMS, Königsbrücker Str. 178, 01099 Dresden, Germany

[a]Electronic mail: maximilian.lederer@ipms.fraunhofer.de

ABSTRACT

The local crystal phase and orientation of ferroelectric grains inside $TiN/Hf_{0.5}Zr_{0.5}O_2/TiN$ have been studied by the analysis of the local electron beam scattering Kikuchi patterns, recorded in transmission. Evidence was found that the ferroelectric phase of the layers is derived from an orthorhombic phase, most likely of space group $Pca2_1$. The orientation analysis reveals a strong out-of-plane texture of the polycrystalline film which is in accordance with a high remanent polarization P_r observed for P-V measurements. The results of this analysis help us to further optimize the ratio of ferroelectric grains and their orientation for many applications, e.g., in the field of emerging memory or infrared sensors.

Published under license by AIP Publishing. https://doi.org/10.1063/1.5129318

Highly textured ferroelectric films are required for high density nonvolatile memories such as ferroelectric field-effect transistors (FeFET),[1] ferroelectric random-access memories (FeRAM),[2] and ferroelectric tunneling junctions (FTJs).[3] Since the discovery of ferroelectricity in ultrathin layers of Si doped HfO_2,[4] ferroelectric properties have been demonstrated in polycrystalline HfO_2 films doped with various elements such as Y, Sr, Al, Si, or Zr.[3] Even undoped HfO_2 has been reported to exhibit ferroelectric properties,[5] which proves that ferroelectricity is an intrinsic property of the confined material.

HfO_2 is fully compatible with conventional complementary metal-oxide semiconductor (CMOS) processes and can be manufactured using many approaches, including atomic layer deposition (ALD). Therefore, it may prove superior to traditional perovskite structure based ferroelectric materials with regard to the applicability in ferroelectric devices. So far, highly scaled FeFETs with thin ferroelectric HfO_2 layers have been fabricated at 28 nm[6] and 22 nm[7] technology node high-k metal gate (HKMG) CMOS processes. Furthermore, the observed piezoelectric[8] and pyroelectric[9] properties reveal potential for future nanoelectromechanical systems (NEMS) and sensor applications.

It has been reported that the ferroelectricity of HfO_2 originates from the orthorhombic phase with the space group $Pca2_1$[10] [Fig. 1(a)]. As this is a metastable phase, a multitude of different crystallographic phases and associated textures can be present in the films, which is influenced by external conditions such as stress,[11] doping,[3] thermal treatment,[12] and film thickness.[13]

Besides the phase of space group $Pca2_1$, two other orthorhombic phases, with the space group Pbca and Pnma, respectively, have been reported in the literature. These two phases are stabilized by high pressure, but they do have an inversion center which does not allow ferroelectricity.[11]

However, the local orientation of the HfO_2 grains as well as their crystallographic phase is of vital importance with regard to its ferroelectric as well as its associated piezoelectric and pyroelectric properties both for materials science and practical applications.

In this article, the analysis of the local electron back-scattering diffraction (EBSD) patterns is used to reveal the crystallographic phase and its local orientation. In contrast to conventional EBSD, transmission-EBSD, also called low-energy transmission Kikuchi diffraction (TKD), enables the analysis of thin films in the nanometer scale. Furthermore, the lateral spatial resolution is strongly improved, thus allowing to obtain indexable EBSD patterns for lateral grain sizes down to 10 nm as demonstrated by Keller and Geiss.[14] They suggested it could help us to determine the phase of more complex crystal structures due to the increased resolution of the finer structure within the diffraction pattern.[14] This originates from the narrower energy distribution of the transmitted electrons.[14]

Published under license by AIP Publishing

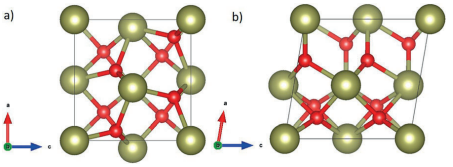

FIG. 1. The crystal structure of hafnium oxide for (a) the ferroelectric orthorhombic ($Pca2_1$) and (b) the monoclinic ($P2_1/c$) phase as calculated by DFT.

The investigated sample was prepared by depositing 10 nm TiN on a highly p-doped silicon wafer using ALD followed by the deposition of 10 nm $Hf_{0.5}Zr_{0.5}O_2$ (HZO) via ALD at 250 °C using $HfCl_4$ and $ZrCl_4$ precursors. After physical vapor deposition (PVD) of a 10 nm TiN capping layer, the sample was annealed at 800 °C utilizing a rapid thermal spike process.

For the electrical analysis of the metal-ferroelectric-metal (MFM) capacitors, the structures were patterned by depositing metal (Ti/Pt) contacts using a shadow mask with a subsequent SC1 TiN wet etch. Dynamic hysteresis measurements (DHM) with an amplitude of 3 V and a frequency of 1 kHz were conducted using an aixACCT TF Analyzer 3000 measurement setup. Cycling pulses were performed with the same amplitude and frequency. For the grazing incidence X-ray diffraction (GIXRD) scan, a Bruker D8 Discover XRD system was utilized, collecting patterns in a 2θ range between 10° and 90° at a fixed incident angle of 0.5°.

Using a dimple grinder, the sample was prepared for the TKD measurement. The TKD measurement was performed in a scanning electron microscope (SEM) with a Bruker Optimus TKD detector. The sample is located perpendicular to the beam, with the detector positioned below the sample [Fig. 2(a)]. The applied accelerating voltage was 30 kV. As the scattered electrons are likely to exit the sample at Bragg conditions, the resulting patterns on the detector are determined by the local periodicity of the material before leaving the sample.[14] Since the electron beam transmits first through the TiN top electrode layer followed by the HZO layer before leaving the sample, the Kikuchi patterns of the TiN crystal structure should appear in the form of an increased noise level or weak artifacts in the detector image.

Kikuchi patterns, as shown in Fig. 2(b), were measured for each point in the scanned region. By taking the scatter signal intensity at every position, a visualization, called quality map, can be constructed

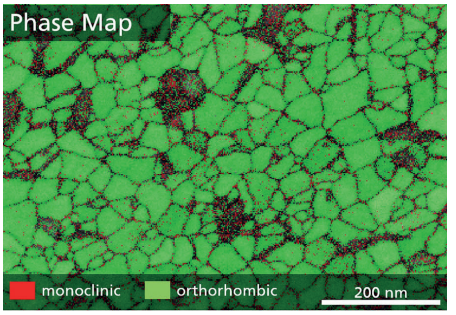

FIG. 3. The phase of local grains is identified from the fitted Kikuchi patterns. Due to fitting with monoclinic and orthorhombic phase only, tetragonal/cubic grains could have been identified as orthorhombic.

[Fig. 2(c)]. Here, individual grains can already be distinguished. Large angle grain boundaries appear as black lines due to their low symmetry, whereas crystalline grains appear white due to their higher symmetry. Since the measurement is performed in transmission, grain boundaries appear sharp as most grain radii exceed the layer thickness, thus being present in a columnar like shape.

In order to extract the crystallographic phase of the individual grains, the detector image undergoes a Hough transformation, which allows us to detect lines and extract their position and orientation. Next, the simulated Kikuchi patterns of the monoclinic ($P2_1/c$) as well as the ferroelectric orthorhombic ($Pca2_1$) phase were compared and oriented to the extracted ones. As shown by the green and red lines in Fig. 2(b), respectively, the aligned theoretical patterns of the two phases fit well with the measured detector image of two representative positions. By performing this for each measurement point, the so-called phase map can be extracted (Fig. 3). It should be noted that TKD does not allow us to determine the lack of an inversion center. Therefore, the space group cannot be uniquely determined.

When comparing these results with the polarization-voltage (P-V) hysteresis loops measured by DHM [Fig. 4(a)], the high fraction of orthorhombic phase fits well with the high remanent polarization (P_r) found after wake-up of the sample. Furthermore, the TKD results are supported by the GIXRD pattern shown in Fig. 4(b). Here, strong

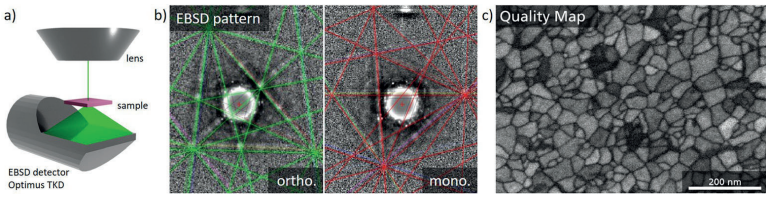

FIG. 2. Transmission Kikuchi diffraction of HZO. A schematic of the experimental setup is given in (a). The measured detector image for two positions is given in (b). The appearing Kikuchi pattern can be fitted with the theoretical Kikuchi lines calculated from the given crystal structures, shown as green lines for the orthorhombic phase and as red lines for the monoclinic phase. The quality map (c) visualizes the contrast of the detector image, thus displaying the grain image.

Published under license by AIP Publishing

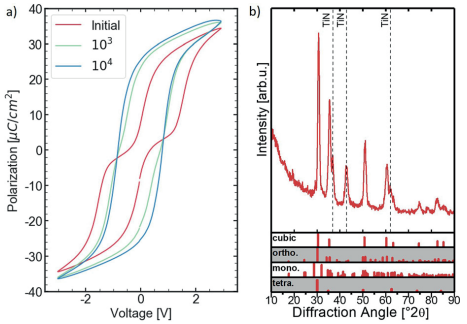

FIG. 4. P-V hysteresis loops (a) and GIXRD pattern (b) of the $Hf_{0.5}Zr_{0.5}O_2$ sample. The hysteresis opens during field cycling (wake-up effect). Afterward, the measured remanent polarization reaches a high value of about 27 $\mu C/cm^2$, indicating a high orthorhombic phase fraction. The GIXRD pattern shows diffraction lines at the expected position for the orthorhombic phase, whereas the expected peaks for the monoclinic phase do not appear clearly. Thus, an insignificant fraction of monoclinic phase is expected.

intensities appear at the expected diffraction lines for orhorhombic/tetragonal/cubic phase, whereas the diffraction lines for monoclinic phase are not distinguishable from the noise. However, the P-V hysteresis loops as well as the GIXRD pattern do not allow us to extract the local and accurate phase distribution. On the contrary, this can be realized by TKD measurements as shown in Fig. 3.

In Fig. 5, the grain size distribution of the monoclinic and orthorhombic phase is displayed. The mean equivalent diameter of the orthorhombic grains lies at about 29 nm, ranging from about 10-70 nm, whereas the monoclinic grains have a mean grain size of about 34 nm, with grain sizes down to about 20 nm. The presence of monoclinic phase in larger grains is in agreement with the predictions made by density functional theory (DFT) calculations of thermodynamics of the HfO_2 material system.[11] This is attributed to the monoclinic phase being the most stable phase of bulk hafnium oxide.[11] By taking into account the surface energy, DFT calculations have shown that for small grain sizes the tetragonal phase is more stable. Furthermore, it has been reported that the orthorhombic phase is only favored at the thermodynamical boundary between monoclinic and tetragonal phase with a narrow range of grain radii smaller than 2.5 nm.[15] With increasing temperature, the stable region of the orthorhombic phase closes and the tetragonal phase is favored for increasing grain sizes.[11]

The high amount of orthorhombic grains larger than the expected 2.5 nm can be explained by kinetics. Due to the high energy barrier for the phase transformation from tetragonal to monoclinic, this transition is suppressed. On the other hand, the energy barrier of the phase transition from tetragonal to orthorhombic is much smaller.[11] As the sample is annealed by RTP, small tetragonal nuclei in the amorphous matrix will grow at high temperatures. Upon cooldown, the tetragonal phase becomes unstable for large grains and switches to the orthorhombic phase.[15] Since the monoclinic phase is favored for larger grains, some of them can overcome the energy barrier and switch to monoclinic upon cooldown, thus explaining the grain distribution presented in Fig. 5 consisting of 3.2% monoclinic and 95.0% orthorhombic grains.

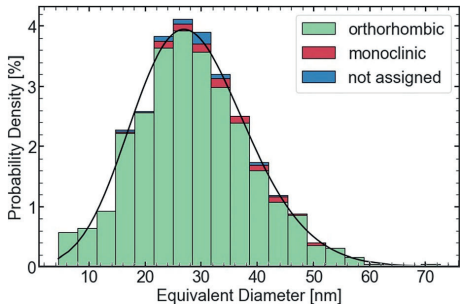

FIG. 5. Grain size distribution of the monoclinic and orthorhombic phase. The grain size distribution is extracted from the phase and quality map. Grains smaller than 5 nm are disregarded. The overall grain size distribution fits well with a lognormal distribution.

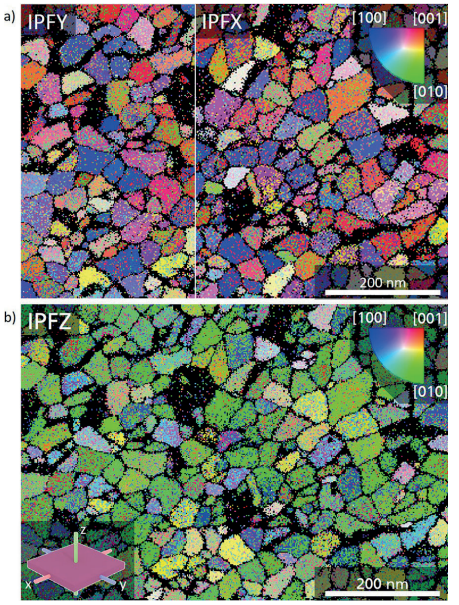

FIG. 6. Grain orientation along the x-/y- and z-axis of the sample (IPFX/IPFY (a) and IPFZ (b) map, respectively). Visualized is the grain orientation extracted from the Kikuchi pattern by color coding of the unit cell axis which is parallel to the respective sample-axis. For the HZO sample, many grains are present with the [010]-axis pointing out-of-plane (along the z-axis), thus indicating a film texture.

Published under license by AIP Publishing

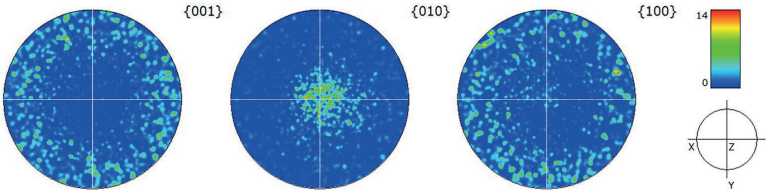

FIG. 7. Stereographic projection of the crystal planes. The {010}-planes are mostly oriented perpendicular to the z-axis of the sample. Consequently, most of the {100}- and {001}-planes are oriented parallel to the z-axis. Yet, in contrast to the {010}-planes, they do not have a texture inside the xy-orientations of the sample.

Besides phase identification, TKD enables the orientation mapping of nanocrystalline materials.[16] With the extracted grain orientation, the pole figure (PF)/inverse pole figure (IPF) of each measurement point can be calculated. Taking the three sample planes, the orientation of the orthorhombic grains can be visualized as the so-called IPF-maps (Fig. 6). The xy-plane, which describes the out-of-plane directions of the thin film, shows a clear texture, whereas the xz/yz-planes show no in-plane texture. Accordingly, most grains are oriented with the [010]-axis pointing out-of-plane.

The origin for the texture could be explained by stress conditions during the crystallization and phase transitions. Recent findings by Schenk *et al.* for La doped HfO_2 also report a textured polycrystalline film with the longest axis lying in-plane. They suggested that the hafnium oxide layer compensates tensile stress during cooldown by aligning the longest axis in-plane.[17] Since the phase transition from the tetragonal phase will occur upon cooldown, tensile stress conditions promote a preferred alignment of the longer unit cell axes to be lying in-plane. As [010] is the shortest axis of the $Pca2_1$ unit cell, the out-of-plane texture should be related to the [010]-axis.

This behavior can be seen in the PFs of the unit cell axes (Fig. 7). The short [010]-axis lies mostly in the z-direction, whereas the longer [100]- and [001]-axis lie randomly oriented in-plane of the thin film.

Since the [001]-axis, which resembles the polarization axis, would lie closely aligned with the in-plane direction, a low remanent polarization would be expected for the sample. On the contrary, P-V results show a high P_r after wake-up. An explanation for this can be derived from the published data on epitaxial films.[18,19] The [010]-axis of their film is oriented perpendicular to the films surface after growth. During the electroforming step, they found that the [010]- and [001]-axes switch, thus resulting in an out-of-plane orientation of the polarization axis.[19] This agrees with the measured P-V data [Fig. 4(a)] as the initial hysteresis is pinched strongly, but it opens up with subsequent cycling. Furthermore, the TKD measurement was performed on the film before wake-up. Consequently, this is a strong indication that also in ferroelectric polycrystalline HfO_2 films, the [010]- and [001]-axes are switching during the wake-up effect.

In conclusion, it is demonstrated that transmission Kikuchi diffraction enables a high-resolution, local, and accurate measurement of the phase fraction of HfO_2. Furthermore, the crystallographic orientation of individual grains is determined, thus allowing us to investigate the texture of the hafnium oxide thin film. By applying this technique to a HZO thin film, it is found that the monoclinic phase is only present in a small fraction of relatively large size grains (3.2% of the total grain count), whereas the ferroelectric orthorhombic phase is present in the full range of grain sizes. This is in agreement with theories based on the thermodynamic and kinetic nature of doped hafnium oxide. Furthermore, an out-of-plane texture of the [010]-axis was found in the polycrystalline film, which can be explained by persistent tensile strain during the annealing step. Combined with electrical data, this suggests a switching of the [010]- and the polar [001]-axis during wake-up in ferroelectric polycrystalline HfO_2 films.

This research was supported by the ECSEL Joint Undertaking project WAKeMeUP in collaboration with the European Union's H2020 Framework Program (No. H2020/2014-2020) and National Authorities under Grant Agreement No. 783176. Furthermore, we received technical support from Bruker and Globalfoundries.

REFERENCES

[1] S. Müller, J. Müller, R. Hoffmann, E. Yurchuk, T. Schlosser, R. Boschke, J. Paul, M. Goldbach, T. Herrmann, A. Zaka, U. Schröder, and T. Mikolajick, IEEE Trans. Electron Devices **60**, 4199 (2013).
[2] J. Müller, T. S. Böscke, S. Müller, E. Yurchuk, P. Polakowski, J. Paul, D. Martin, T. Schenk, K. Khullar, A. Kersch, W. Weinreich, S. Riedel, K. Seidel, A. Kumar, T. M. Arruda, S. V. Kalinin, T. Schlosser, R. Boschke, R. van Bentum, U. Schröder, and T. Mikolajick, in IEDM (2013), pp. 10.8.1–10.8.4.
[3] J. Müller, P. Polakowski, S. Müller, and T. Mikolajick, ECS J. Solid State Sci. Technol. **4**, N30 (2015).
[4] T. S. Böscke, J. Müller, D. Bräuhaus, U. Schröder, and U. Böttger, Appl. Phys. Lett. **99**, 102903 (2011).
[5] P. Polakowski and J. Müller, Appl. Phys. Lett. **106**, 232905 (2015).
[6] J. Müller, E. Yurchuk, T. Schlosser, J. Paul, R. Hoffmann, S. Muller, D. Martin, S. Slesazeck, P. Polakowski, J. Sundqvist, M. Czernohorsky, K. Seidel, P. Kucher, R. Boschke, M. Trentzsch, K. Gebauer, U. Schroder, and T. Mikolajick, in VLSI (2012), pp. 25–26.
[7] S. Dunkel, M. Trentzsch, R. Richter, P. Moll, C. Fuchs, O. Gehring, M. Majer, S. Wittek, B. Muller, T. Melde, H. Mulaosmanovic, S. Slesazeck, S. Muller, J. Ocker, M. Noack, D.-A. Lohr, P. Polakowski, J. Muller, T. Mikolajick, J. Hontschel, B. Rice, J. Pellerin, and S. Beyer, in IEDM (2017), pp. 19.7.1–19.7.4.
[8] P. Buragohain, C. Richter, T. Schenk, H. Lu, T. Mikolajick, U. Schroeder, and A. Gruverman, Appl. Phys. Lett. **112**, 222901 (2018).
[9] C. Mart, T. Kämpfe, S. Zybell, and W. Weinreich, Appl. Phys. Lett. **112**, 052905 (2018).
[10] X. Sang, E. D. Grimley, T. Schenk, U. Schroeder, and J. M. LeBeau, Appl. Phys. Lett. **106**, 162905 (2015).
[11] R. Materlik, C. Künneth, and A. Kersch, J. Appl. Phys. **117**, 134109 (2015).
[12] L. Xu, T. Nishimura, S. Shibayama, T. Yajima, S. Migita, and A. Toriumi, J. Appl. Phys. **122**, 124104 (2017).

Published under license by AIP Publishing

[13]E. Yurchuk, J. Müller, S. Knebel, J. Sundqvist, A. P. Graham, T. Melde, U. Schröder, and T. Mikolajick, Thin Solid Films **533**, 88 (2013).
[14]R. R. Keller and R. H. Geiss, J. Microsc. **245**, 245 (2012).
[15]M. H. Park, Y. H. Lee, H. J. Kim, Y. J. Kim, T. Moon, K. D. Kim, S. D. Hyun, T. Mikolajick, U. Schröder, and C. S. Hwang, Nanoscale **10**, 716 (2018).
[16]P. W. Trimby, Ultramicroscopy **120**, 16 (2012).
[17]T. Schenk, C. M. Fancher, M. H. Park, C. Richter, C. Künneth, A. Kersch, J. L. Jones, T. Mikolajick, and U. Schroeder, Adv. Electron. Mater. **5**, 1900303 (2019).
[18]T. Shimizu, K. Katayama, T. Kiguchi, A. Akama, T. J. Konno, and H. Funakubo, Appl. Phys. Lett. **107**, 032910 (2015).
[19]T. Shimizu, T. Mimura, T. Kiguchi, T. Shiraishi, T. J. Konno, Y. Katsuya, O. Sakata, and H. Funakubo, Appl. Phys. Lett. **113**, 212901 (2018).

Published under license by AIP Publishing

2.3 TEXTURE ANALYSIS ON SILICON INTERFACE LAYERS

Besides capacitor-based memory concepts (see Sec. 3.1 for more information), where the ferroelectric is located between two metallic electrodes[4], HfO_2 can also appear sandwiched between a bottom SiO_2 on top of silicon and a top TiN electrode. This case is apparent in ferroelectric field effect transistors (FeFETs), where HfO_2 acts as the gate oxide as commonly the case for the gate stack in high-k metal gate (HKMG) technology (see Sec. 4.1). FeFETs structured in this manner were already integrated into the 28 nm and 22 nm technology node. To better understand how this oxide interface layer (IL) impacts the crystallization process and, therefore, the microstructure generation, we analyzed various HfO_2 layers, particularly Si-doped hafnium oxide (HSO) layers as commonly used in FeFETs using TKD [68, 69].

It could be observed that the orthorhombic phase also dominates in these layers, with only some residual grains being monoclinic. For the crystallographic analysis we assume the tetragonal phase to be omitted, due to its Curie temperature between 250°C and 500 °C. Furthermore, cubic and rhombohedral phases were excluded since being less stable than the orthorhombic phase, as theoretically backed up by density functional theory (DFT). Without this simplification, an analysis of the TKD diffraction images would not be feasible due to the very subtle difference in their crystallographic structure.

The samples have been verified to reveal strongly ferroelectric behavior by initial dynamic hysteresis measurements. In contrast to the previously reported microstructures of HSO and HZO metal–ferroelectric–metal (MFM) structures as discussed in Sec. 2.2, where disc-shaped grains were found, here dendritic grain formation occurred, which suggests a very different crystallization process. Furthermore, the dendritic grains appear to be much larger with a mean of about $232 - 244$ nm independent of anneal temperature. This finding has a strong influence in the study of FeFETs with respect to device-to-device variation and short-channel devices. Due to the large crystallite size with high orthorhombic phase fraction a highly uniform device formation is possible.

Importantly, when investigating the pole figures it was shown that the [010]-axis does not align fully parallel, as we have observed for the MFM structures, but appears donut-shaped. The [110]-axis appears to align parallel to this axis. This analysis shows, that the preferred crystal orientation of the crystallites is significantly tilted to the out-of-plane direction, which for instance increases the required switching field applied perpendicularly to the film. However, for FeFET

4 Here preferably TiN or W for microelectronic applications are used

applications, such a configuration also significantly lowers the depolarization field, which is expected to stabilize the ferroelectric polarization state and increase the retention time [70].

A possibility to reduce improve the influence of the microstructure is the use of heterostructures of thinner HfO_2 films stacked with the insertion of oxide thin films like Al_2O_3 resulting in smaller grain sizes [71].

PUBLICATION: Impact of the SiO_2 interface layer on the crystallographic texture of ferroelectric hafnium oxide

PUBLICATION DETAILS The following publication is reproduced with permission from: M. Lederer, A. Reck, K. Mertens, R. Olivo, P. Bagul, A. Kia, B. Volkmann, T. Kämpfe, K. Seidel, and L. M. Eng, "Impact of the SiO2 interface layer on the crystallographic texture of ferroelectric hafnium oxide", Applied Physics Letters 118, 012901, (2021). Copyright 2021 American Physical Society.

Applied Physics Letters ARTICLE scitation.org/journal/apl

Impact of the SiO_2 interface layer on the crystallographic texture of ferroelectric hafnium oxide

Cite as: Appl. Phys. Lett. **118**, 012901 (2021); doi: 10.1063/5.0029635
Submitted: 15 September 2020 · Accepted: 19 December 2020 ·
Published Online: 4 January 2021

View Online Export Citation CrossMark

M. Lederer,[1,a)] A. Reck,[1] K. Mertens,[1] R. Olivo,[1] P. Bagul,[1] A. Kia,[1] B. Volkmann,[2] T. Kämpfe,[1] K. Seidel,[1] and L. M. Eng[3]

AFFILIATIONS

[1]Fraunhofer IPMS, Königsbrücker Str. 178, 01099 Dresden, Germany
[2]GLOBALFOUNDRIES Fab 1 LLC & Co. KG, Dresden 01109, Germany
[3]Institut für Angewandte Physik, Technische Universität Dresden, 01069 Dresden, Germany

Note: This paper is part of the Special Topic on Materials and Devices Utilizing Ferroelectricity in Halfnium Oxide.
[a)]**Author to whom correspondence should be addressed:** maximilian.lederer@ipms.fraunhofer.de

ABSTRACT

Applying transmission Kikuchi diffraction (TKD) allows us to fundamentally investigate the Si-doped-hafnium-oxide (HSO) microstructure that results from the interface layer present in ferroelectric field-effect transistors. In addition to the predominant orthorhombic phase, dendritic HSO grains larger than 100 nm govern the microstructure composition. Furthermore, the observed strong out-of-plane texture aligned along the [110] and [011] axis clearly differs from features found in hafnium oxide thin films grown on TiN layers. Our TKD analysis shows that the texture intensity strongly varies for samples annealed at different temperatures. Additionally, intra-granular misorientation and chemical composition analyses of the layers provide insight into the crystallization process of these ferroelectric thin films.

Published by AIP Publishing. https://doi.org/10.1063/5.0029635

Transmission Kikuchi diffraction (TKD) enables the microstructure analysis of ultra-thin films, including local crystallographic phase and orientation mapping.[1,2] This method recently has been beautifully demonstrated as a powerful tool for ferroelectric hafnium oxide analysis,[3] which certainly spurs research interest in a broad range of applications, e.g., nonvolatile memories or pyroelectric sensors.[4,5]

Ferroelectricity in hafnium oxide has been demonstrated to originate from the orthorhombic phase with space group $Pca2_1$.[6] This metastable phase can be stabilized, e.g., by doping[7,8] or when applying mechanical stress due to the presence of a capping layer.[9] Nevertheless, the microstructure may contain grains of other polymorphs like the monoclinic ($P2_1/c$) phase, which represents the thermodynamic ground state.[10]

The large coercive field, superior thickness scaling below the 5 nm threshold, and complementary-metal–oxide–semiconductor (CMOS) process compatibility for ferroelectric HfO_2 make these thin films superior to classical perovskite-based ferroelectrics such as lead titanate zirconate, for instance, in nonvolatile memory applications.[11] More specifically, this already enabled realizing one-transistor (1T)-based ferroelectric memories, namely, ferroelectric field-effect transistors (FeFETs).[12] Compared to capacitor-based memory concepts where the ferroelectric is located between two metallic electrodes, preferably TiN, HfO_2 in FeFETs is introduced directly into the gate stack with the HfO_2 typically being sandwiched in-between the bottom SiO_2 interface layer (covering the semiconductor surface) and the top TiN electrode. FeFETs structured in this manner were already integrated into the 28 nm and 22 nm node technology.[13,14]

For investigating how this interface layer impacts the crystallization process and, therefore, the microstructure, we analyze here Si-doped hafnium oxide (HSO) layers in the aforementioned layer stack annealed at different temperatures using TKD. All samples are produced by atomic layer deposition (ALD) of HSO onto highly p-doped Si wafers covered with a native oxide layer. Here, $HfCl_4$ and $SiCl_4$ are used as precursors in a cycle ratio of 16:1. Electrodes are formed via physical vapor deposition of TiN. The crystallization anneal is performed by rapid thermal processing at 650 °C, 800 °C, and 1000 °C.

TKD measurements on dimpled samples are carried out using a Bruker Optimus TKD detector head mounted into a scanning electron microscope. The acceleration voltage is 30 kV and a current of 3.2 nA is used. The details on the measurement method and data processing

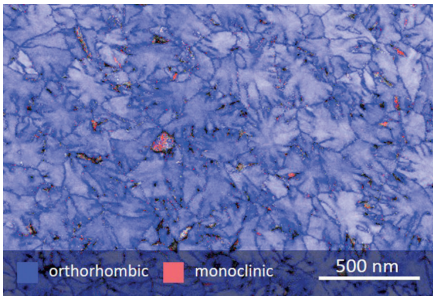

FIG. 1. Microstructure and crystallographic phase distribution of the Si-doped hafnium oxide layer annealed at 650 °C. Most grains are of dendritic shape in the orthorhombic phase (blue color), while only a small amount of monoclinic grains is found (red). Note that the tetragonal, cubic, and rhombohedral phases were not analyzed here.

have been shown in a previous work.[3] Additionally, grazing-incident X-ray diffraction (GIXRD) measurements were performed with 2θ ranging from 15° to 45° in 0.1° steps. The chemical composition of the films is analyzed with time-of-flight secondary-ion-mass-spectrometry (ToF-SIMS). Capacitor structures were formed by shadow-mask-based deposition of Ti/Pt contacts and subsequent wet etch.

The grain structure of the HSO layers appears very clearly in the quality/phase map, as depicted in Fig. 1 for the HSO sample annealed at 650 °C. As seen, the orthorhombic phase (blue color) dominates, with some residual grains being monoclinic (red color). Note that the tetragonal phase has not been taken into account, since the Curie temperature lies between 250 °C and 500 °C.[16–18] Furthermore, cubic and rhombohedral phases were excluded since being less stable than the orthorhombic phase, as theoretically backed up by density functional theory.[10,19,20] Furthermore, initial dynamic hysteresis measurements on pristine capacitor structures revealed ferroelectric behavior with high polarization values [see Fig. 2(a)]. In contrast to the previously reported microstructures of HSO and Zr-doped hafnium oxide (HZO) metal–ferroelectric–metal (MFM) structures[3,15] finding disc-shaped columnar grains, dendritic grains are detected here in the metal–ferroelectric–insulator–semiconductor (MFIS) structures.

In addition to a value of 52 nm, the average equivalent grain size of MFM samples weighted by area[15] is significantly smaller than the one measured for the MFIS samples, having values between 232 nm and 244 nm [see Fig. 2(b)]. Since both MFM and MFIS samples were annealed under similar conditions, the observed strong differences in precipitation must be clearly related to the substrate layer in use, i.e., the amorphous SiO_2 and the polycrystalline ALD TiN layer with a slight (111) texture.[21] Consequently, various effects might impact the crystallization behavior, such as changes in the local mechanical stress field resulting from different thermal expansion coefficients of the materials, or variation in the nucleation behavior, e.g., heterogeneous and homogeneous nucleation. Bagmut *et al.* stated that the onset of crystalline phase formation in HfO_2 initiates at higher temperature when using amorphous substrates instead of (poly)crystalline ones.[22] In addition, island (IPC) and dendrite (DPC) polymorphic growth were reported for zirconium and hafnium oxides, with IPC or DPC nucleating in the cubic/tetragonal or orthorhombic/monoclinic phase, respectively.[22–24]

When comparing samples that have been annealed at different temperatures, the average grain size remains constant and no clear trend with temperature is observed. This is quite remarkable, as crystal growth generally is very temperature sensitive due to on-surface diffusion. Notably, monoclinic grains show this temperature dependence, and their fraction grows with increasing temperature [see Fig. 2(c)]. In samples annealed at 650 °C, only a low number of grains is monoclinic (see Fig. 1), with this fraction significantly growing for elevated annealing temperatures. This is exactly seen from Fig. 2(c) when plotting the equivalent grain diameter vs annealing temperature.

A possible explanation for this behavior is the phase transformation of amorphous HfO_2 reported by Bagmut,[24] which proceeds in two steps: first, orthorhombic grains grow up to a critical grain diameter D^* above which they transform into the monoclinic phase. The reported values for D^* range from 143 nm to 294 nm (Ref. 24) and are comparable to the average grain sizes reported in this work here. As the transition to the monoclinic phase involves unit-cell shearing (that, notably, is mechanically suppressed when using TiN capping layers[7]) we believe that this phase transition in MFIS structures is shifted to higher temperatures, with some larger grains already being

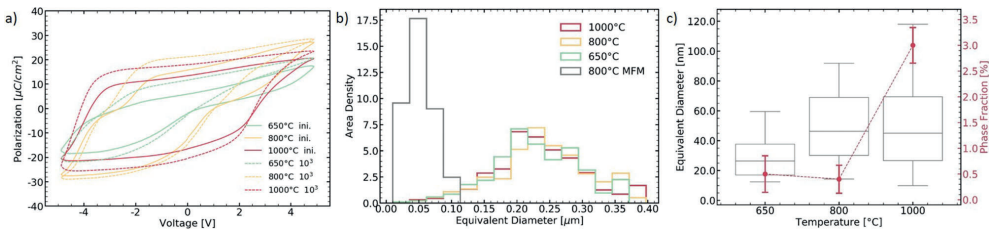

FIG. 2. Polarization response and grain size distribution of HSO in MFIS structures annealed at different temperatures: (a) ferroelectric behavior observed by dynamic hysteresis measurements with an amplitude of 5 V at 1 kHz for the pristine and cycled film. Electric field cycling is performed under identical conditions. (b) The distribution of the equivalent diameter, weighted by area, shows a strong increase in grain size for MFIS samples as compared to the HSO MFM sample (as reported earlier[15]). The annealing temperature seems to have no impact on the grain size; (c) both the extracted equivalent grain diameter in the monoclinic phase and the monoclinic phase fraction increase with elevated annealing temperature.

TABLE I. Crystallographic texture, grain size, and shape of HSO-based MFM and MFIS structures, respectively.

Substrate	Ferroelectric	Anneal	Average grain size (weighted by area)	Grain shape	Out-of-plane texture
ALD TiN, polycrystalline, (111) texture[21]	ALD HSO 10 nm (Ref. 15)	800 °C (Ref. 15)	52 nm (Ref. 15)	Disc-shaped[15]	[010][15]
SiO_2, amorphous	ALD HSO 10 nm	650 °C–1000 °C	232 nm–244 nm	Dendritic	[110] and [011]

rendered monoclinic. In addition to the two-stage process, the nucleation of the monoclinic phase has been demonstrated experimentally as well[24] and may also explain the small monoclinic grains present in all samples here.

The strong differences in the HSO microstructure for MFM and MFIS samples (as summarized in Table I) are further underlined when analyzing their crystallographic texture. While an out-of-plane texture of the [002]- and [020]-axis was reported for HSO and HZO MFM samples,[3,15,25] a different texture is observed on the MFIS stacks. As shown with the inverse pole figure (IPF) maps in Fig. 3(a), MFIS samples annealed at 1000 °C indicate a clear out-of-plane texture as well. Some grains aligned closely to the [010]- or [001]-axis appear with dots or larger connected regions of the [001]- or [010]-axis, respectively, a signature that can be easily assigned to either misindexing or ferroelasticity, as these are the axes that most likely undergo ferroelastic switching.[26]

For a detailed analysis of the out-of-plane texture, pole figures are extracted [see Fig. 3(b)]. Here, the [010]-axis does not align fully parallel but rather donut-shaped around the out-of-plane axis of the sample. Instead, the [110]- and [011]-axis align parallel to this axis. Furthermore, the [111]-axis shows a weak texture aligning either parallel or perpendicular to the normal vector of the thin film. This would result in a tilted polarization axis after wake-up and, therefore, in an increase in the effective coercive field of the layer. A similar orientation of the polarization axis has also been reported for a 22-nm FeFET.[15]

With decreasing annealing temperature, this texture becomes less dominant while more [111]- and [101]-axes align out-of-plane [see Fig. 3(c)]. This agrees well with the measured GIXRD patterns [see Fig. 3(d)], where an increased intensity of the diffraction line at 24°, corresponding to the (110) index, is observed for the 1000 °C anneal. Minor shifts of the diffraction lines to higher angles are likely to originate from strain inside the layer. Nevertheless, a texture that might be described by a preferred absence of all ⟨100⟩ axes is very surprising for a layer grown on an amorphous substrate, as no orientational information can be transferred to the hafnium oxide. Moreover, the polymorphic phase transitions that HfO_2 is likely to undergo would not enable the formation of such a texture.

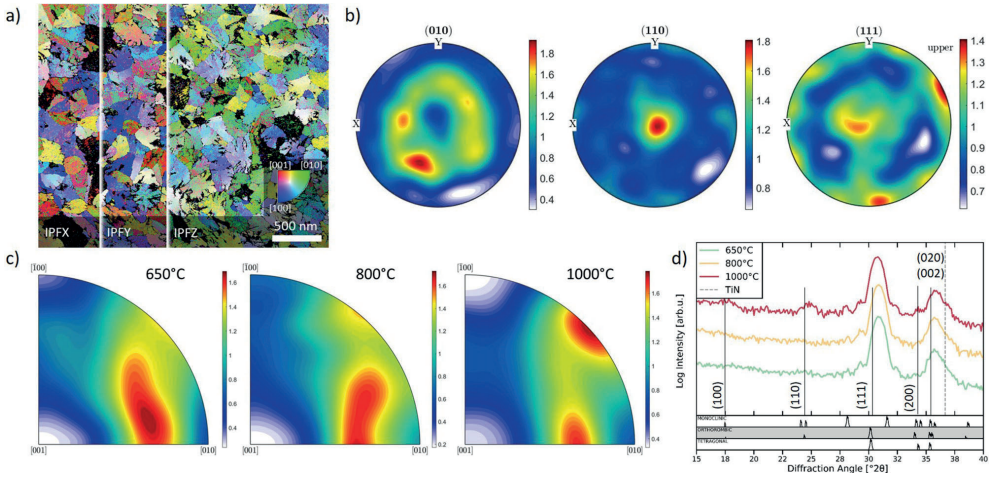

FIG. 3. TKD microstructure analysis: (a) inverse pole figure maps of the x, y, and z planes for the sample annealed at 1000 °C highlight the presence of an out-of-plane texture; (b) pole figures of the same sample indicate the sample normal vector to be [110] aligned; (c) inverse pole figures of the z plane show an increasing texture along the [110] and [011] axes when raising the annealing temperature. Samples annealed at lower temperature also show [111]- and [101]-axis alignment; and (d) accompanying GIXRD patterns supporting our TKD results.